

Article

Bioisosteric discovery of NPA101.3, a second generation RET/VEGFR2 inhibitor optimized for single-agent polypharmacology

Marialuisa Moccia, Brendan Frett, Lingtain Zhang, Naga Rajiv Lakkaniga, David C Briggs, Rakhee Chauhan, Annalisa Brescia, Giorgia Federico, Wei Yan, Massimo Santoro, Neil Q McDonald, Hong-yu Li, and francesca carlomagno

J. Med. Chem., **Just Accepted Manuscript** • DOI: 10.1021/acs.jmedchem.9b01336 • Publication Date (Web): 16 Apr 2020

Downloaded from pubs.acs.org on April 18, 2020

Just Accepted

"Just Accepted" manuscripts have been peer-reviewed and accepted for publication. They are posted online prior to technical editing, formatting for publication and author proofing. The American Chemical Society provides "Just Accepted" as a service to the research community to expedite the dissemination of scientific material as soon as possible after acceptance. "Just Accepted" manuscripts appear in full in PDF format accompanied by an HTML abstract. "Just Accepted" manuscripts have been fully peer reviewed, but should not be considered the official version of record. They are citable by the Digital Object Identifier (DOI®). "Just Accepted" is an optional service offered to authors. Therefore, the "Just Accepted" Web site may not include all articles that will be published in the journal. After a manuscript is technically edited and formatted, it will be removed from the "Just Accepted" Web site and published as an ASAP article. Note that technical editing may introduce minor changes to the manuscript text and/or graphics which could affect content, and all legal disclaimers and ethical guidelines that apply to the journal pertain. ACS cannot be held responsible for errors or consequences arising from the use of information contained in these "Just Accepted" manuscripts.

**Bioisosteric discovery of NPA101.3, a second generation RET/VEGFR2 inhibitor
optimized for single-agent polypharmacology**

Marialuisa Moccia,^{1,†} Brendan Frett,^{2,6,†} Lingtian Zhang,² Naga Rajiv Lakkaniga,²
David C. Briggs,³ Rakhee Chauhan,³ Annalisa Brescia,¹ Giorgia Federico,¹ Wei Yan,²
Massimo Santoro,¹ Neil Q. McDonald,^{3,4} Hong-yu Li,^{2,6*} and Francesca
Carlomagno^{1,5*}

†Marialuisa Moccia and Brendan Frett contributed equally to this work.

¹Dipartimento di Medicina Molecolare e Biotecnologie Mediche, Università di Napoli
"Federico II", 80131, Napoli, Italia; ²Department of Pharmaceutical Sciences, College
of Pharmacy, University of Arkansas for Medical Sciences, Little Rock, AR 72205,
USA; ³Signalling and Structural Biology Laboratory, The Francis Crick Institute,
London, NW1 1AT UK; ⁴Institute of Structural and Molecular Biology, Department of
Biological Sciences, Birkbeck College, London, WC1E 7HX, UK; ⁵Istituto di
Endocrinologia ed Oncologia Sperimentale del CNR, 80131, Napoli, Italia; ⁶Synactix
Pharmaceuticals, Inc., Tucson, AZ 85718, USA.

1
2
3
4 ***Corresponding Authors:** Hong-yu Li, Department of Pharmaceutical Sciences,
5
6
7 College of Pharmacy, University of Arkansas for Medical Sciences, Little Rock, AR
8
9
10 72205, United States; (Ph. 5012961154; HLi2@uams.edu); Francesca Carlomagno,
11
12
13 Dipartimento di Medicina Molecolare e Biotecnologie Mediche, Università di Napoli
14
15
16 "Federico II" via S. Pansini 5, 80131 Napoli-Italy (Ph. +390815455561; Fax:
17
18
19
20
21 +390817462685; francesca.carlomagno@unina.it)
22
23
24
25
26
27

28 **Keywords:** kinase; tyrosine kinase inhibitor; targeted therapy; thyroid cancer; lung
29
30
31 adenocarcinoma.
32
33
34
35
36
37
38
39
40
41
42
43
44
45
46
47
48
49
50
51
52
53
54
55
56
57
58
59
60

ABSTRACT

RET receptor tyrosine kinase is a driver oncogene in human cancer. We recently identified the clinical drug candidate Pz-1, which targets RET and VEGFR2. A key *in vivo* metabolite of Pz-1 is its less active demethylated pyrazole analogue. Using bioisosteric substitution methods, here, we report the identification of NPA101.3, lacking the structural liability for demethylation. NPA101.3 showed selective inhibitory profile and an inhibitory concentration 50 (IC₅₀) of <0.001 μ M for both RET and VEGFR2. NPA101.3 inhibited phosphorylation of all tested RET oncoproteins as well as VEGFR2 and proliferation of cells transformed by RET. Oral administration of NPA101.3 (10 mg/kg/day) completely prevented formation of tumours induced by RET/C634Y-transformed cells, while it decreased, but did not abrogate, formation of tumours induced by a control oncogene (HRAS/G12V). The balanced synchronous inhibition of both RET and VEGFR2, as well the resistance to demethylation, renders NPA101.3 a potential clinical candidate for RET-driven cancers.

INTRODUCTION

RET (REarranged during Transfection) is the receptor tyrosine kinase (RTK) for neurotrophic factors of the GDNF (glial cell line-derived neurotrophic factor) family (1). In several human cancers, RET rearrangements lead to the formation of chimeric oncoproteins, containing the RET tyrosine-kinase (TK) domain fused to the N-terminal region of heterologous proteins. These include: papillary thyroid carcinoma (PTC) (2), medullary thyroid carcinoma (MTC) (3), lung adenocarcinoma (4-6), chronic myeloproliferative disorders (7, 8), Spitz melanoma (9), colon (10, 11), breast (12) and salivary duct (13) carcinomas. CCDC6 (coiled-coil domain containing 6)-RET rearrangement has also been found in EGFR (epidermal growth factor receptor) mutant lung adenocarcinoma patients who had progressed upon EGFR TKI treatment (14). In addition, various types of germline point mutations activating the RET kinase are the causative event of hereditary MTC, in the frame of multiple endocrine neoplasia type 2 (MEN2A, MEN2B) syndromes. Somatic RET mutations, mostly RET/M918T, are commonly associated (around 50% of cases) to sporadic MTC (1, 15). Finally, RET is overexpressed in several malignancies including breast (16, 17) and pancreatic (18, 19) carcinoma.

RET targeting with tyrosine kinase inhibitors (TKIs) has emerged as a promising molecular approach for the treatment of cancer (20, 21). Two TKIs, Vandetanib and Cabozantinib, were found to exhibit VEGFR2 (vascular endothelial growth factor receptor 2) and RET activity (22, 23). These two drugs have been approved to treat MTC because of their capability to prolong progression-free survival (24, 25). In addition, Sorafenib and Lenvatinib, two multikinase inhibitors with activity against RET, have been approved for the treatment of radioiodine-refractory differentiated thyroid cancer (26, 27). Novel TKIs, BLU-667, LOXO-292 and RXDX-105, have recently demonstrated promising clinical activity in RET-driven cancers (28-30).

Toxicity, due to on- or off-targets effects, and resistance formation may limit efficacy of TKIs in clinical practice. We sought out to set up a fragment-based chemical screen to identify novel RET inhibitors. This approach lead to the clinical candidate Pz-1, a type-2 TKI directed against RET and VEGFR2 (31).

In vivo stability is a critical factor that directly determines efficacy (32). Through completion of investigative new drug (IND) studies, a demethylated less active metabolite of Pz-1 was identified. Here, by applying bioisosteric substitution of the

1
2
3
4 Pz-1 site susceptible to demethylation, we report the identification of NPA101.3, as a
5
6
7 novel clinical TKI candidate and its characterization through *in vitro* and *in vivo*
8
9
10 assays.
11
12
13
14
15
16
17
18
19
20
21
22
23
24
25
26
27
28
29
30
31
32
33
34
35
36
37
38
39
40
41
42
43
44
45
46
47
48
49
50
51
52
53
54
55
56
57
58
59
60

RESULTS

Discovery of NPA101.3. During IND-studies of Pz-1, a series of *in vivo* metabolites were identified; via Phase 1 metabolic systems, Pz-1 is oxidized, hydrolysed, or demethylated generating a less active derivative (Fig. 1 and data not shown). Hydrolysis and initial oxidation occur at the selectivity region, which is the region of Pz-1 that enters the allosteric pocket of both RET and VEGFR2. Any modification to reduce metabolism at this region can alter selectivity and inhibitory profiles and, therefore is likely to alter the optimized RET/VEGFR2 inhibitory profile. Another major, metabolic pathway of Pz-1 is initiated via the Phase 1 demethylation of methylpyrazole to generate Pz-1a. In turn, Pz-1a is further biotransformed via oxidation (to Pz-1b) or oxidation and sugar conjugation through Phase 2 systems (to Pz-1c). Interestingly, the methylpyrazole substituent of Pz-1 is oriented towards the solvent and is not expected to contribute significantly to selectivity profiles (31, 32) (Fig. 1).

Bioisosteric replacement of the methylpyrazole of Pz-1 was investigated to generate an alternative clinical candidate with similar polypharmacological profile but resistance to demethylation. In both RET and VEGFR2, the methylpyrazole binds to

solvent exposed regions, which can accommodate a variety of substituents. SAR (structure-activity relationship) studies have shown that replacement of methylpyrazole with various five-member ring systems decreases inhibitory activity (31). Therefore, substitution with polar, electron-deficient (methylsulfonyl)benzene was investigated. The methylsulfonyl group occupies the same chemical space as the methyl pyrazole and has the same hydrogen binding pattern at the computer modelling (data not shown); therefore, it is expected not to affect the pharmacological activity of the drug as compared to methylpyrazole. Importantly, analogues containing (methylsulfonyl)benzene do not carry the structural liability of demethylation. Therefore, the (methylsulfonyl)benzene was chosen as an appropriate bioisosteric replacement for methylpyrazole, to obtain the novel compound designated NPA101.3 (Fig. 1). The chemical synthesis of NPA101.3 is described in the Supporting information.

Computational modelling of NPA101.3. NPA101.3 was modelled in the RET kinase DFG (aspartic acid [D892], phenylalanine [F893], glycine [G894])-out computational model as previously described (Fig. 2) (31). The model suggested that NPA101.3

binds to RET kinase in its inactive (DFG-out) conformation, as it is characteristic of type-2 TKIs (33). The benzimidazole moiety acts as the 'warhead', making a key hydrogen bond with A807 at the RET ATP binding site (hinge-region). The benzimidazole also forms two π - π stacking interactions with Y806. The *p*-sulfone substituent displays orientation towards the solvent and engages K728 through a cation- π interaction. The amide region interacts with D892 from the DFG motif through a hydrogen bond. This interaction opens-up a novel lipophilic pocket, which is effectively filled by *tert*-butyl isoxazole. The modelling predicted NPA101.3 to bind RET with high affinity and with a projected ΔG of -11.9 k/cal mol. Moreover, the model indicated that binding of NPA101.3 was not influenced by substitutions of V804, which is the gatekeeper residue whose replacement with a methionine or a leucine confers resistance to Vandetanib, Cabozantinib, and several other inhibitors (Fig. 2 and Supporting Information, Table S1) (29, 34-36). NPA101.3 was also predicted to bind VEGFR2 with comparable high affinity (Fig. 2). Indeed, similar to Pz-1, the free rotation of the methylene linker permits tailored orientation of the isoxazole in the allosteric pocket of both RET and VEGFR2 enabling balanced inhibition of both kinases (31).

To further address the type of binding, we docked sorafenib in the RET model and compared docking poses between the RET-sorafenib and VEGFR2-sorafenib (PDB #3WZE) complexes. The poses were near-identical, further suggesting NPA101.3 is a type-2 inhibitor (Supporting information, Fig. S1).

Kinase inhibitory activity of NPA101.3. We tested the ability of NPA101.3 to inhibit RET, the RET/V804M mutant, and VEGFR2 in an *in vitro* kinase assay. To determine if NPA101.3 tightly bound the kinase, we used high concentration of ATP (190 μ M). Such a high concentration is orders of magnitude greater than the K_m for either RET or VEGFR2 and reflects the high intracellular concentration of ATP (1-10 mM). NPA101.3 exhibited an inhibitory concentration 50 (IC_{50}) of 0.001 μ M for RET, 0.008 μ M for RET/V804M, and 0.003 μ M for VEGFR2. Thus, NPA101.3 represents a novel RET/VEGFR2 dual inhibitor with a pharmacological profile similar to Pz-1.

To further investigate NPA101.3 binding to RET, a thermal shift assay was performed to monitor protein melting temperature. This assay determines the drug-induced increase in the melting temperature (ΔT_m) of the isolated RET kinase domain, which reflects the stability of the kinase-ligand complex (37, 38) and

correlates with the inhibitor IC_{50} (39). Addition of NPA101.3 increased the thermal stability of active and phosphorylated RET by a dramatic ΔT_m of $16^\circ\text{C} \pm 1.1^\circ\text{C}$, over a time course of 240 minutes (Fig. 3C; a representative experiment is reported in Fig. 3A). This was consistent with values seen for type-2 inhibitors, such as Sorafenib, stabilising a DFG-out inactive conformer (40). We observed the same magnitude of thermal shift by NPA101.3 for wild type and V804M (Fig. 3B), confirming that the compound is insensitive to gatekeeper mutation. In contrast, a substantially smaller ΔT_m shift of $6.1^\circ\text{C} \pm 3.3^\circ\text{C}$ was observed with the type-1 compound PP1 (Fig. 3C), consistent with our previous published data (38). As expected, the type-1 inhibitor PP1 was sensitive to gatekeeper mutation (Fig. 3C). We conclude that NPA101.3 binds tightly to both wild type and V804M RET kinase domain in a type-2 binding mode.

In addition, NPA101.3, at a concentration of 100 nM, was subjected to a kinome scan against a 96 kinases panel representing major kinome clusters (Supporting Information, Table S2). The compound featured good selectivity, displaying strong binding activity (>90% bound) for only 7 additional kinases: CSF1R (colony stimulating factor 1 receptor), FRK (fyn related Src family tyrosine kinase),

HCK (HCK proto-oncogene, Src family tyrosine kinase), LYN (lyn proto-oncogene, Src family tyrosine kinase), MKNK2 (MAPK interacting serine/threonine kinase 2), TRKA (neurotrophic receptor tyrosine kinase 1) and TRKC (neurotrophic receptor tyrosine kinase 3) and weak binding (>10-35% bound) for another 6 kinases (Supporting information Table S2 and Fig. S2). It is important to note that measurement of binding affinity, that is based on control-ligand displacement (K_d), is more sensitive than the *in vitro* kinase assay. Among the 7 kinases with >90% binding, TRKA and CSF1R were selected for an *in vitro* kinase assay. NPA101.3 was active against TRKA and CSF1R with IC_{50} of 32 nM and 46 nM, respectively (Supporting information, Fig. S3). Finally, we verified the ability of NPA101.3 to interfere with hERG (potassium voltage-gated channel subfamily H member 2) conductivity via patch-clamp assay. As shown in Supporting information, Table S4, the IC_{50} dose of NPA101.3 for hERG was 7.57 μ M (while it was 0.027 μ M in the case of the positive control E-4031), thereby more than 7000-fold higher than that for RET (1 nM) (Supporting information, Table S3).

NPA101.3-mediated inhibition of RET and VEGFR2 phosphorylation and signalling.

Fibroblasts transfected with RET/C634R were treated with increasing doses of NPA101.3, ranging from 0.1 to 10.0 nM. RET autophosphorylation was assessed by Western blotting using two different antibodies able to recognize phosphorylated Y905, located in the RET kinase activation loop, or Y1062, a multidocking site involved in RET downstream signalling (41). As shown in Figure 4A, RET phosphorylation started to be inhibited at 0.3 nM and was almost completely blocked at 3.0 nM. NPA101.3 also inhibited other MTC-associated RET oncogenic point mutants, including RET/M918T, RET/A883F, and RET/V804L/M (Fig. 4B). Rearranged RET oncoproteins (CCDC6-RET, NCOA4-RET, FGFR1OP-RET) were highly sensitive to NPA101.3 inhibition, as well (Fig. 4C). Finally, 1.0 nM NPA101.3 reduced ligand-induced VEGFR2 autophosphorylation; inhibition was virtually total at 10.0 nM, indicating that NPA101.3 has similar inhibitory activity for VEGFR2 and RET (Fig. 4D).

NPA101.3 inhibited RET autophosphorylation and signalling along the SHC/MAPK pathway in human cancer cell lines endogenously expressing RET oncogenic variants, including MTC cell lines, TT (RET/C634W) and MZ-CRC-1

(RET/M918T), PTC cell line TPC-1 (CCDC6-RET); in the lung adenocarcinoma cell line Lc-2/ad (CCDC6-RET) only RET and SHC (but not MAPK) de-phosphorylation was detectable (Supporting information, Fig. S4). Virtually no effect on SHC/MAPK signalling was identified in control cell lines lacking RET oncogenes, including Nthy-ori-3.1 thyroid follicular cells, BCPAP and 8505-C, derived from thyroid cancers negative for RET oncogenes, and PC-9, A549 and CALU-1, derived from lung adenocarcinomas negative for RET oncogenes (Supporting information, Fig. S5).

NPA101.3-mediated inhibition of RET-driven cell proliferation. The murine pro-B cell line Ba/F3 requires IL-3 (interleukin 3) for proliferation and survival; this dependency is bypassed by active tyrosine kinases. Therefore, the Ba/F3 cell line is a standard cell culture model to determine activity and drug-mediated inhibition of tyrosine kinases (42). Accordingly, stable transfection of RET/C634R, RET/M918T and CCDC6-RET oncoproteins promotes IL-3-independent growth (Fig. 5). Treatment with NPA101.3 blunted RET-driven (IC_{50} of 1.6-3.1 nM), but not IL-3-driven parental Ba/F3 cell proliferation (Fig. 5), parallel to inhibition of RET phosphorylation (Supporting information Fig. S6).

1
2
3 NPA101.3 inhibited proliferation of RET mutant TT, MZ-CRC-1, TPC-1 and Lc-
4
5
6
7 2/ad human cancer cells with an IC_{50} of 0.67-3.6 nM (Supporting information, Fig. S7
8
9
10 and Table S4). The IC_{50} dose for all human RET-negative cells was greater than
11
12
13 100.0 nM, confirming compound selectivity (Supporting information, Fig. S8 and
14
15
16
17 Table S4).
18
19
20
21
22

23 **NPA101.3 inhibits tumorigenicity of RET-transformed cells.** The IC_{50} dose for
24
25
26 NPA101.3-mediated NIH3T3 RET/C634Y cell proliferation inhibition was 4.17 nM;
27
28
29 virtually no effect was observed on proliferation of NIH3T3 HRAS (Harvey rat
30
31
32 sarcoma virus oncogene)/G12V cells up to 100.0 nM (Supporting information Fig.
33
34
35
36
37 S9). At 10.0 nM, the compound almost completely inhibited phosphorylation of RET
38
39
40 and SHC, and attenuated phosphorylation of MAPK, in NIH3T3 RET/C634Y cells,
41
42
43 while virtually no effect was detectable in NIH3T3 HRAS/G12V cells up to a dose of
44
45
46
47 100.0 nM (Supporting information Fig. S10).
48
49
50

51 *In vivo* target (RET and VEGFR2) inhibition was studied by treating animals
52
53
54 grafted with NIH3T3 RET/C634Y cells at different doses (0.3, 1 or 3 mg/kg/day p.o.)
55
56
57
58 of NPA101.3 for two days and then performing Western blot analysis on protein
59
60

1
2
3 extracts. As shown in Supporting information (Fig. S11) 3 mg/kg/day dose of
4
5
6
7 NPA101.3 strongly inhibited RET autophosphorylation and signalling as well as
8
9
10 VEGFR2 phosphorylation. Then, in order to determine anti-tumorigenic activity and
11
12
13 to better distinguish RET- and VEGFR2-mediated effects, we tested NPA101.3 in
14
15
16
17 nude mice transplanted with NIH3T3 cells transformed either by RET/C634Y or
18
19
20 HRAS/G12V. Before tumours appeared, animals were treated daily with NPA101.3
21
22
23 (1.0, 3.0 or 10.0 mg/kg/day) or left untreated. NPA101.3 preferentially inhibited RET
24
25
26 compared to RAS-driven tumours. While 10.0 mg/kg of compound completely
27
28
29 prevented tumor formation induced by oncogenic RET, the treatment reduced, but
30
31
32 did not abrogate, formation of tumours driven by RAS; moreover, at lower doses the
33
34
35 compound significantly reduced growth of RET-, but not RAS-, driven tumors (Fig. 6).
36
37
38
39
40
41 At 1.0 mg/kg, NPA101.3 exhibited strong RET phosphorylation and signalling
42
43
44 inhibition in NIH3T3 RET/C634Y tumours (Supporting information Fig. S12); in
45
46
47 contrast, virtually no effect on RAS signalling (MAPK phosphorylation) was detected
48
49
50
51 in NIH3T3 HRAS/G12V tumours. Still, VEGFR2 inhibition was detected also in RAS-
52
53
54 driven tumours, an effect that may explain the, albeit reduced, drug effect on their
55
56
57 growth (Supporting information Fig. S13). Importantly, as predicted, no trace of
58
59
60

1
2
3 NPA101.3 de-methyl metabolites was detected after 1 or 4 hours from oral dosing in
4
5
6
7 mice (Supporting information Fig. S14). Moreover, in terms of potential toxicity, no
8
9
10 significant change in standard blood markers of organ damage was detected upon 7
11
12
13 days of oral dosing (10 mg/Kg/day) of NPA101.3, indicating that at this dose the
14
15
16
17 compound had no general toxicity (Supporting information Fig. S15).
18
19
20
21
22
23
24
25
26
27
28
29
30
31
32
33
34
35
36
37
38
39
40
41
42
43
44
45
46
47
48
49
50
51
52
53
54
55
56
57
58
59
60

DISCUSSION AND CONCLUSIONS

Drug efficacy of a clinical agent is determined by target inhibition and ADMET (adsorption, distribution, metabolism, excretion, and toxicity) profiles (32). During the IND study of the clinical TKI candidate Pz-1, we identified a major, metabolic pathway initiated by Phase 1 demethylation of the Pz-1 methylpyrazole substituent. Here, in order to generate secondary candidates with similar pharmacological profiles to Pz-1 but no propensity to demethylation, we replaced methylpyrazole with the metabolically-resistant bioisostere (methylsulfonyl)benzene. This led to NPA101.3, a demethylation-resistant clinical candidate optimized for single-agent polypharmacology.

Molecular modelling indicated that, similar to Pz-1, NPA101.3 binds the DFG-out 'inactive' conformation of RET and VEGFR2, thus functioning as a *bona fide* type-2 TKI (31). This is supported experimentally by the relatively large thermal shift observed for the RET kinase-NPA101.3 complex. NPA101.3 exhibited an IC_{50} of 0.001 μ M for RET and 0.003 μ M for VEGFR2. Noteworthy, similar to Pz-1, NPA101.3 was able to bind tightly to and inhibit (IC_{50} of 0.008 μ M) the RET mutant at the gatekeeper site (V804M), which is refractory to the clinical inhibitors Vandetanib and

1
2
3 Cabozantinib (31). NPA101.3 featured excellent selectivity for RET and VEGFR2,
4
5
6
7 exhibiting affinity only for few other kinases such as TRKs (TRKA and TRKC),
8
9
10 CSF1R, FRK, HCK, LYN and MKNK2. Among them, TRKA and TRKC are well known
11
12
13 driver oncogenes, which expands the potential therapeutic application of NPA101.3
14
15
16
17 beyond RET-driven cancers (43).
18
19

20
21 In cell-based assays, NPA101.3 inhibited RET autophosphorylation and
22
23
24 displayed a potent (IC_{50} between 0.67 and 4.17 nM) growth inhibitory effect on
25
26
27 different types of RET (either transfected or endogenously expressing) mutant cells
28
29
30 with no detectable effect at doses up to 100 nM in cells negative for RET oncogenes.
31
32
33
34 Finally, NPA101.3 featured efficacy already at 1 mg/kg/day in RET-driven tumours in
35
36
37 nude mice. At higher doses (10 mg/kg/day), NPA101.3 displayed activity also against
38
39
40 RAS-driven tumours, likely mediated by VEGFR2 inhibition. Therefore, though in a
41
42
43 therapeutic setting toxicity may be increased by hitting multiple targets, it is feasible
44
45
46 that activity of the NPA101.3 against RET-driven tumours, may take advantage from
47
48
49 a combination of cell autonomous (on tumour cells growth mediated by RET
50
51
52 inhibition) and non-cell autonomous (on blood vessels formation mediated by
53
54
55 VEGFR2 inhibition) effects, potentiating its effect and reducing the chances of
56
57
58
59
60

1
2
3 resistance development. Several TKIs with anti-RET activity are available and some
4
5
6
7 are already registered for treatment of different types of thyroid cancers. Lesson
8
9
10 learned from the use of TKIs in various cancer types has shown that second line
11
12
13 inhibitors are clinically useful when first line treatments are hampered by toxicity
14
15
16 and/or resistance. Based on potency, selectivity, and balanced RET/VEGFR2
17
18
19 inhibition, we posit that NPA101.3 may represent a promising, demethylation-
20
21
22 resistant type-2 TKI for the treatment of RET-driven tumours. Studies regarding PK
23
24
25
26
27
28 () profile and metabolic stability will clarify in the future how NPA101.3 is metabolized
29
30
31
32 *in vivo*. This notion will be crucial to propose NPA101.3 as a clinical candidate.
33
34
35
36
37
38
39
40
41
42
43
44
45
46
47
48
49
50
51
52
53
54
55
56
57
58
59
60

EXPERIMENTAL SECTION

General chemistry procedures and synthesis of NPA101.3. Molecular formula Smiles

String: O=C(NC1=NOC(C(C)(C)C)=C1)CC(C=C2)=CC=C2N(C=N3)C4=C3C=C(C5

=CC=C(S(=O)(C)=O)C=C5)C=C4) All solvents were reagent grade or HPLC grade

and all starting materials were obtained from commercial sources and used without

further purification. Purity of final compounds was assessed using a Shimadzu ultra-

high throughput LC/MS system (SIL-20A, LC-20AD, LC-MS 2020, Phenomenex®

Onyx Monolithic C-18 Column) at variable wavelengths of 254 nm and 214 nm

(Shimadzu PDA Detector, SPD-MN20A) and was >95%, unless otherwise noted. The

HPLC mobile phase consisted of a water-acetonitrile gradient buffered with 0.1%

formic acid. ¹H NMR spectra were recorded at 400 MHz and ¹³C spectra were

recorded at 100 MHz, both completed on a Varian 400 MHz instrument (Model#

4001S41ASP). All compounds were purified using silica gel (0.035-0.070 mm, 60 Å)

flash chromatography, unless otherwise noted. Microwave assisted reactions were

completed in sealed vessels using a Biotage Initiator microwave synthesizer.

***In vitro* kinase assays.** Kinase activity was measured by a microfluidic assay that monitors the separation of the phosphorylated product from substrate (31). The assay was run using a 12-sipper chip on a Caliper EZ Reader II (PerkinElmer®, Waltham, USA) with separation buffer (100 mM HEPES, 10 mM EDTA, 0.015% Brij-35, 0.1% CR-3 PerkinElmer®). In 96-well polypropylene plates (Greiner, Frickenhausen, Germany), compound stocks (20 mM in DMSO) were diluted into kinase buffer (50 mM HEPES, 0.075% Brij-35, 0.1 % Tween 20, 2 mM DTT, 10 mM MgCl₂, and 0.02% NaN₃) in 12-point $\frac{1}{2}$ log dilutions (2 mM–6.32 nM). After, 1 μ L was transferred into a 384-well polypropylene assay plate (Greiner). The enzymes (RET, RET/V804M, VEGFR2, TRKA, CSF1R) (Invitrogen™, Grand Island, USA) were diluted in kinase buffer to a concentration of 2 nM and 5 μ L of the enzyme mixture was transferred to the assay plate. Kinases were pre-incubated with the TKI or control buffer, with gentle shaking for 60 min to allow the inhibitor to trap the DFG-out conformation; indeed, it has been reported for the type-2 (DFG-out) p38 inhibitor, BIRB-796, that an increase in incubation time increases activity (44). A substrate mix was prepared containing ATP (Ambresco®, Solon, USA) and substrate peptide dissolved in kinase buffer, and 5 μ L of the substrate mix was added to the assay plate. Running concentrations were

as follows: ATP (190 μ M), peptide (1.5 μ M), compound 12-point $\frac{1}{2}$ log dilutions (0.2 mM–0.632 nM). For positive control, no inhibitor was added. For negative control, no enzyme was added. The plate was run until 10–20% conversion, based on the positive control wells. The following separation conditions were utilized: upstream voltage - 500V; downstream voltage, -1900V; chip pressure -0.8. Percent inhibition was measured for each well comparing starting peptide to phosphorylated product peaks relative to the baseline. Dose response curves, spanning the IC_{50} dose, were generated in GraphPad Prism® 7 and fit to an exponential one-phase decay line; IC_{50} values were obtained from the half-life value of the curve. IC_{50} values were generated in triplicate.

Thermal shift assay. Wild type and V804M mutant RET core kinase domain proteins were expressed in SF21 cells and purified using a GST affinity tag as previously described (45). Subsequently, both proteins were purified and phosphorylated. The affinity tag was removed using HRV 3C protease. To determine the protein thermal shifts, 3 μ M recombinant proteins were incubated with DMSO (vehicle control), NPA101.3, PP1 or Sorafenib (in 100% DMSO), with a final drug concentration of

1
2
3 40 μ M, and a final DMSO concentration of 1% (v/v). Sypro-Orange dye (Life
4
5
6
7 Technologies) was added to each drug treatment, and the thermal shift was
8
9
10 measured in a QuantStudio 12K Flex Real-Time PCR System (Applied Biosystems)
11
12
13 over a temperature range of 25–90 °C. Subsequent analysis was performed using
14
15
16
17 Protein Thermal Shift Software v1.2 (Applied Biosystems).
18
19
20
21
22
23

24 **Cell cultures.** NPA101.3 was dissolved in dimethyl sulfoxide (DMSO) at 50 mM
25
26
27 concentration and stored at -80°C. Final dosing solution was prepared on the day of
28
29
30 use by dilution of the stock solution in cell growth media. RAT1 cells transformed by
31
32
33 the various RET mutants (46) were a kind gift of M. Billaud and were cultured in
34
35
36
37 DMEM with 10% foetal calf serum, 2 mM L-glutamine and 100 units/ml penicillin-
38
39
40 streptomycin (GIBCO). NIH3T3 cells transformed by RET/C634Y, HRAS/G12V,
41
42
43
44 CCDC6-RET, NCOA4-RET and FGFR1OP-RET were cultured in DMEM with 5% calf
45
46
47 serum, 2 mM L-glutamine and 100 units/mL penicillin-streptomycin (GIBCO).
48
49
50
51 Parental NIH3T3 cells were grown in DMEM with 10% calf serum, 2 mM L-glutamine
52
53
54 and 100 units/mL penicillin-streptomycin (GIBCO). All the RET constructs expressed
55
56
57
58 in RAT1 or NIH3T3 cells encoded the short isoform of the RET protein (RET-9). Ba/F3
59
60

1
2
3 murine pro-B cells stably expressing NCOA4-RET, RET/C634R and RET/M918T
4
5
6
7 mutant proteins (all cloned in the long RET-51 isoform) were generated by
8
9
10 electroporation. Parental and transformed Ba/F3 cells were cultured in RPMI
11
12
13 supplemented with 10% foetal calf serum, 2 mM L-glutamine and 100 units/ml
14
15
16
17 penicillin-streptomycin (GIBCO), and, in the case of parental cells, supplemented with
18
19
20 10 ng/ml IL-3. CALU-1, derived from a human lung adenocarcinoma, were grown in
21
22
23
24 EMEM with 10% foetal calf serum, 2 mM L-glutamine and 100 units/mL penicillin-
25
26
27 streptomycin (GIBCO). PC-9, derived from a human lung adenocarcinoma, were
28
29
30 grown in RPMI with 10% foetal calf serum, 2 mM L-glutamine and 100 units/mL
31
32
33
34 penicillin-streptomycin. Nthy-ori-3-1, derived from normal thyroid follicular tissue and
35
36
37 immortalized by SV40 Large T, TPC-1, derived from a human PTC harbouring
38
39
40
41 CCDC6-RET (47), BCPAP, derived from human PTC, 8505-C, derived from a human
42
43
44 undifferentiated thyroid cancer, and A549, derived from a human lung
45
46
47
48 adenocarcinoma, were cultured in DMEM with 10% foetal calf serum, 2 mM L-
49
50
51 glutamine and 100 units/mL penicillin-streptomycin. TT, from a human MTC
52
53
54 harbouring RET/C634W (48), and MZ-CRC-1, from a human MTC harbouring
55
56
57 RET/M918T (a kind gift of R. F. Gagel), were cultured in RPMI with 20% foetal calf
58
59
60

serum, 2 mM L-glutamine and 100 units/mL penicillin-streptomycin (GIBCO). Lc-2/ad, derived from human lung adenocarcinoma harbouring CCDC6-RET (49), were grown in RPMI 1640/Ham's F12 (1:1) with 10% foetal calf serum, 2 mM L-glutamine and 100 units/mL penicillin-streptomycin (GIBCO). All the human cell lines were SNP authenticated in 2017.

Immunoblotting. Protein lysates were prepared according to standard procedures.

Briefly, cells were lysed in a buffer containing 50 mM N-2-hydroxyethylpiperazine-N'-2-ethanesulfonic acid (HEPES; pH 7.5), 1% (vol/vol) Triton X-100, 150 mM NaCl, 5 mM EGTA, 50 mM NaF, 20 mM sodium pyrophosphate, 1 mM sodium vanadate, 2 mM phenylmethylsulphonyl fluoride (PMSF) and 1 µg/mL aprotinin. Lysates were clarified by centrifugation at 10,000 Xg for 15 min. Lysates containing comparable amounts of proteins, estimated by a modified Bradford assay (Bio-Rad, Munich, Germany), were subjected to direct Western blot. Immune complexes were detected with the enhanced chemiluminescence kit (Amersham Pharmacia Biotech, Little Chalfort, UK). Anti-phospho-SHC (#Y317), that recognizes SHC protein when phosphorylated on Y317, was from Upstate Biotechnology Inc. (Lake Placid, NY).

Anti-SHC (H-108) was from Santa Cruz Biotechnology (Santa Cruz, CA). Anti-MAPK (#9101) and anti-phospho-MAPK (#9102), specific for p42/44MAPK (ERK1/2) phosphorylated on Thr202/Tyr204, were from Cell Signalling (Danvers, MA, USA). Anti-phospho-VEGFR2/KDR (#2478), specific for VEGFR2/KDR phosphorylated on Tyr1175 and anti-VEGFR2/KDR (#2479) were from Cell Signalling Technologies (Danvers, MA, USA). Anti-phospho-p70S6K (#9234), specific for p70S6K phosphorylated on Thr389 and anti-p70S6K (#2708) were from Cell Signalling Technologies (Danvers, MA, USA). Anti-RET is a polyclonal antibody raised against the tyrosine kinase protein fragment of human RET; anti-phospho905 is a phospho-specific polyclonal antibody recognizing RET proteins phosphorylated at Y905 and anti-phospho1062 is a phospho-specific polyclonal antibody recognizing RET proteins phosphorylated at Y1062 (50). Secondary antibodies coupled to horseradish peroxidase were from Santa Cruz Biotechnology.

Cell growth curves. Nthy-ory-3-1 (10,000/well), TPC-1 (10,000/well), MZ-CRC-1 (100,000/well), TT (200,000/well), Lc-2/ad (100,000/well), BCPAP (10,000/well), 8505-C (10,000/well), PC-9 (10,000/well), A549 (10,000/well), CALU-1 (10,000/well),

NIH3T3 RET/C634Y (10,000/well) and NIH3T3 HRAS/G12V (10,000/well) were seeded in 6-well tissue culture plates. Cells were kept in 2% (TPC-1), 5% (Nthy-ori-3-1), or 10% (BCPAP, 8505-C, CALU-1, A549, PC-9, TT, MZ-CRC-1 and Lc-2/ad) foetal calf serum or in 2% (NIH3T3 RET/C634Y and HRAS/G12V) calf serum. Ba/F3 cells (200,000/well in 2ml) were seeded in 6-well tissue culture plates and kept in 10% foetal calf serum. The day after plating, different concentrations of drug or vehicle were added to the medium and changed every 2-3 days. Cells were counted every day (Ba/F3), 2 days (fibroblasts) or 2-3 days (human cell lines). To compare cell growth, we performed unpaired Student's *t* test using the Instat software program (Graphpad Software Inc). All *P* values were two-sided, and differences were considered statistically significant at *P* < .02. IC₅₀ doses were calculated through a curve fitting analysis from last day of growth curves using the PRISM software program (Graphpad Software Inc).

Mouse xenograft experiments. NPA101.3 was dissolved in 80% H₂O, 19.875% Tween 20, 0.125% Xanthan gum. The formulation was stored at room temperature and vortexed prior to administration. NIH3T3 RET/C634Y (200,000 cells) or NIH3T3

HRAS/G12V (50,000 cells) were inoculated subcutaneously into dorsal portion (both sides) of 6-week-old female BALB/c nu/nu mice (n. 32 mice/cell line) (Jackson Laboratories, Bar Harbor, Maine). After 4 days, before tumours had appeared, animals were randomly assigned to receive NPA101.3 (1.0, 3.0 or 10 mg/kg daily) (8 mice/group) or vehicle control (8 mice) by oral gavage. Tumour diameters were measured with caliper every 2-3 days. Tumour volumes (V) were calculated by the rotational ellipsoid formula: $V = A \times B^2 / 2$ (A=axial diameter; B= rotational diameter). No mouse showed signs of wasting or other signs of toxicity. Animals were fed *ad libitum* on an autoclaved diet and tap water and were maintained at the Dipartimento di Medicina Molecolare e Biotecnologie Mediche Animal Facility. All manipulations were performed while the animals were under isoflurane gas anaesthesia. Animal studies were conducted in accordance with Italian regulations for experimentation on animals and approved by the Italian Ministry of health (Authorization n. 1023/2015-PR). To compare tumour growth the unpaired Student's *t* test (InStat program, GraphPad software) was used. *P* values were statistically significant at *P* < 0.05.

ASSOCIATED CONTENT

Supporting Information

1) Supplementary Methods

- RET DFG-out Homology Model Development
- Molecular modelling
- Kinome scan
- Synthesis of ethyl 2-(4-((4-bromo-2-nitrophenyl)amino)phenyl)acetate (1a),
- Synthesis of ethyl 2-(4-((2-amino-4-bromophenyl)amino)phenyl)acetate (1b),
- Synthesis of ethyl 2-(4-(5-bromo-1H-benzo[d]imidazol-1-yl)phenyl)acetate (1),
- Synthesis of N-(5-(tert-butyl)isoxazol-3-yl)-2-(4-(5-(4-(methylsulfonyl)phenyl)-1H-benzo[d]imidazol-1-yl)phenyl)acetamide (NPA-101.3)
- Patch-Clamp assay
- LC-MS analytic conditions
- Toxicity.

2) Supplementary Tables

- Table S1: ΔG values of NPA101.3 in the RET DFG-out Homology Model with various (Valine 804) Gatekeeper Mutations
- Table S2: NPA101.3 KinomeScan Panel screen,
- Table S3: NPA101.3 inhibition of hERG,
- Table S4: NPA101.3 growth inhibitory effect on human cells.

3) Supplementary Figures

- Figure S1: Docking pose of sorafenib in the RET DFG-out model compared to X-Ray crystal structure of Sorafenib in VEGFR2 (PDB #3WZE)
- Figure S2: NPA101.3 binding selectivity
- Figure S3: RET, TRKA and CSF1R kinase inhibition by NPA101.3
- Figure S4: NPA101.3-mediated inhibition of phosphorylation and signalling of oncogenic RET proteins endogenously expressed in human cancer cells
- Figure S5: Effects of NPA101.3 on RAS/MAPK signalling pathway in RET-negative human cancer cells
- Figure S6: NPA101.3-mediated inhibition of phosphorylation of oncogenic RET proteins expressed in Ba/F3 cells

- Figure S7: NPA101.3-mediated inhibition of proliferation of RET mutant thyroid and lung cancer cells
- Figure S8: Effects of NPA101.3 on proliferation of RET-negative cancer cells
- Figure S9: NPA101.3-mediated inhibition of proliferation of RET-transformed NIH3T3 cells
- Figure S10: NPA101.3-mediated inhibition of phosphorylation and signalling of oncogenic RET proteins expressed in NIH3T3 cells
- Figure S11: *In vivo* target inhibition of NPA101.3 in nude mice implanted with cells transformed by RET/C634Y
- Figure S12: Effects of NPA101.3 on cellular phosphorylation events in nude mice implanted with NIH3T3 cells transformed by RET/C634Y
- Figure S13: Effects of NPA101.3 on cellular phosphorylation events in nude mice implanted with NIH3T3 cells transformed by HRAS/G12V
- Figure S14: *In vivo* metabolism study, biochemical analysis.

Molecular formula string of NPA101.3 is available on-line in the journal site

ACCESSION CODES

- VEGFR2 DFG-out crystal structure (PDB# 2OH4)
- Amino acid sequence of RET (PDB# 2IVU)
- Sorafenib in VEGFR2 DFG-out crystal structure (PDB #3WZE)

AUTHORS INFORMATION

Corresponding authors

Hong-yu Li: HLi2@uams.edu; Francesca
Carlomagno: francesca.carlomagno@unina.it

Author Contributions

Marialuisa Moccia and Brendan Frett contributed equally to this work; Marialuisa Moccia, Annalisa Brescia, Giorgia Federico performed the cell-based and animal-based experiments; Brendan Frett, Lingtian Zhang, Wei Yan, Naga Rajiv Lakkaniga,

Rakhee Chauhan performed the synthesis, the modelling studies and the in vitro kinase assays; David C. Briggs performed the thermal shift assay; Massimo Santoro and Neil Q. McDonald participated to experiment planning and data analysis; Hong-yu Li and Francesca Carlomagno participated to experiment planning and data analysis and wrote the manuscript.

ACKNOWLEDGEMENTS

MZ-CRC-1 cells and RAT1 cells expressing RET mutants were kindly donated by R.F. Gagel (MD Anderson Cancer Center, USA) and by M. Billaud (Institut Albert Bonniot, Grenoble, France), respectively.

ABBREVIATIONS USED

A, alanine; ADMET, adsorption, distribution, metabolism, excretion, and toxicity; C, cysteine; CCDC6, coiled-coil domain containing 6; CSF1R, colony stimulating factor 1 receptor; D, aspartic acid; EGFR, epidermal growth factor receptor; F, phenylalanine; FGFR1OP, fibroblast growth factor receptor 1 oncogene partner; FRK, fyn related Src family tyrosine kinase; G, glycine; GDNF, glial cell line-derived neurotrophic factor; HCK, HCK proto-oncogene, Src family tyrosine kinase; hERG (potassium voltage-gated channel subfamily H member 2); HRAS, Harvey rat sarcoma virus oncogene; IC₅₀, inhibitory concentration 50; IL3, interleukin 3 IND, investigative new drug; K, lysine L, leucine; LYN, LYN proto-oncogene, Src family tyrosine kinase; M, methionine; MAPK, mitogen activated protein kinase; MEN2, multiple endocrine neoplasia type 2; MKNK2, MAPK interacting serine/threonine kinase 2; MTC, medullary thyroid carcinoma; NCOA4, nuclear coactivator 4; PK, pharmacokinetics; PTC, papillary thyroid carcinoma; R, arginine; RET, REarranged during Transfection; RTK, receptor tyrosine kinase; SAR, structure-activity relationship; SHC, SHC adaptor protein 1; T, threonine; TK, tyrosine-kinase; TKI, tyrosine kinase inhibitor; TRKA, neurotrophic receptor tyrosine kinase 1; TRKC, neurotrophic receptor tyrosine kinase 3; V, valine; VEGFR2, vascular endothelial growth factor receptor 2; W, tryptophan; Y, tyrosine.

DISCLOSURE OF POTENTIAL CONFLICTS OF INTEREST

1
2
3 B. Frett and H.Y. Li have ownership interest in Synactix Pharmaceuticals, Inc. F.
4 Carlomagno, B. Frett, M. Santoro, and H.Y. Li are inventors of patent
5 WO/2015/187818. D.C. Briggs, R. Chauhan and N.Q. McDonald declare no potential
6
7 conflicts of interest.
8
9

10 11 12 **FOUNDING SOURCES**

13
14 This study was supported by NIH 1R01CA197178-01A1R grant (to HL). In addition,
15 HL was supported by NIH 1R01CA194094-010 and UAMS start-up funding; FC was
16 supported by the Associazione Italiana per la Ricerca sul Cancro (AIRC); NQM was
17 supported by the Francis Crick Institute, which receives its core funding from Cancer
18 Research UK (FC001115), the UK Medical Research Council (FC001115) and the
19 Wellcome Trust (FC001115). RC was supported by a grant to NQM from the
20 Association for Multiple Endocrine Neoplasia Disorders MTC Research Fund. This
21 work was also supported by an Institutional Development Award (IDeA) from the
22 National Institute of General Medical Sciences of the National Institutes of Health
23 under grant number "P20 GM109005", by the UAMS Seeds of Science cancer
24 research grant and by a grant from the American Thyroid Association (ATA/Thyca)
25 and by the POR Campania FESR 2014-2020 "SATIN" grant
26
27
28
29
30
31
32
33
34
35
36
37
38
39
40
41
42
43
44
45
46
47
48
49
50
51
52
53
54
55
56
57
58
59
60

REFERENCES

- 1) Mulligan, L. M. RET Revisited: Expanding the Oncogenic Portfolio. *Nat. Rev. Cancer* **2014**, *14*, 173-186.
- 2) Cancer Genome Atlas Research Network. Integrated Genomic Characterization of Papillary Thyroid Carcinoma. *Cell* **2014**, *159*, 676-690.
- 3) Grubbs, E. G.; Ng, P. K.; Bui, J.; Busaidy, N. L.; Chen, K.; Lee, J. E.; Lu, X.; Lu, H.; Meric-Bernstam, F.; Mills, G. B.; Palmer, G.; Perrier, N. D.; Scott, K.L.; Shaw, K. R.; Waguespack, S. G.; Williams, M. D.; Yelensky, R.; Cote, G. J. RET Fusion as a Novel Driver of Medullary Thyroid Carcinoma. *J. Clin. Endocrinol. Metab.* **2015**, *100*, 788-793.
- 4) Kohno, T.; Ichikawa, H.; Totoki, Y.; Yasuda, K.; Hiramoto, M.; Nammo, T.; Sakamoto, H.; Tsuta, K.; Furuta, K.; Shimada, Y.; Iwakawa, R.; Ogiwara, H.; Oike, T.; Enari, M.; Schetter, A. J.; Okayama, H.; Haugen, A.; Skaug, V.; Chiku, S.; Yamanaka, I.; Arai, Y.; Watanabe, S.; Sekine, I.; Ogawa, S.; Harris, C. C.; Tsuda, H.; Yoshida, T.; Yokota, J.; Shibata, T. KIF5B-RET Fusions in Lung Adenocarcinoma. *Nat. Med.* **2012**, *18*, 375-377.

- 1
2
3
4 5) Takeuchi, K.; Soda, M.; Togashi, Y.; Suzuki, R.; Sakata, S.; Hatano, S.; Asaka,
5
6
7 R.; Hamanaka, W.; Ninomiya, H.; Uehara, H.; Lim Choi, Y.; Satoh, Y.; Okumura,
8
9
10 S.; Nakagawa, K.; Mano, H.; Ishikawa, Y. RET, ROS1 and ALK Fusions in Lung
11
12
13 Cancer. *Nat. Med.* **2012**, *18*, 378-381.
14
15
16
17 6) Lipson, D.; Capelletti, M.; Yelensky, R.; Otto, G.; Parker, A.; Jarosz, M.; Curran,
18
19
20 J. A.; Balasubramanian, S.; Bloom, T.; Brennan, K. W.; Donahue, A.; Downing, S.
21
22
23 R.; Frampton, G. M.; Garcia, L.; Juhn, F.; Mitchell, K.C.; White, E.; White, J.;
24
25
26 Zwirko, Z.; Peretz, T.; Nechushtan, H.; Soussan-Gutman, L.; Kim, J.; Sasaki, H.;
27
28
29 Kim, H. R.; Park, S. I.; Ercan, D.; Sheehan, C. E.; Ross, J. S.; Cronin, M. T.; Jänne,
30
31
32 P. A.; Stephens, P. J. Identification of New ALK and RET Gene Fusions from
33
34
35 Colorectal and Lung Cancer Biopsies. *Nat Med.* **2012**, *18*, 382-384.
36
37
38
39
40
41 7) Ballerini, P.; Struski, S.; Cresson, C.; Prade, N.; Toujani, S.; Deswarte, C.;
42
43
44 Dobbelstein, S.; Petit, A.; Lapillonne, H.; Gautier, E. F.; Demur, C.; Lippert, E.;
45
46
47 Pages, P.; Mansat-De Mas, V.; Donadieu, J.; Huguet, F.; Dastugue, N.;
48
49
50 Broccardo, C.; Perot, C.; Delabesse, E. RET Fusion Genes are Associated with
51
52
53 Chronic Myelomonocytic Leukemia and Enhance Monocytic Differentiation.
54
55
56
57
58
59 *Leukemia* **2012**, *26*, 2384-2389.
60

- 1
2
3
4 8) Bossi, D.; Carlomagno, F.; Pallavicini, I.; Pruneri, G.; Trubia, M.; Raviele, P. R.;
5
6
7 Marinelli, A.; Anaganti, S.; Cox, M. C.; Viale, G.; Santoro, M.; Di Fiore, P. P.;
8
9
10 Minucci, S. Functional Characterization of a Novel FGFR1OP-RET
11
12
13 Rearrangement in Hematopoietic Malignancies. *Mol. Oncol.* **2014**, *8*, 221-231.
14
15
16
17 9) Wiesner, T.; He, J.; Yelensky, R.; Esteve-Puig, R.; Botton, T.; Yeh, I.; Lipson, D.;
18
19
20 Otto, G.; Brennan, K.; Murali, R.; Garrido, M.; Miller, V. A.; Ross, J. S.; Berger, M.
21
22
23 F.; Sparatta, A.; Palmedo, G.; Cerroni, L.; Busam, K. J.; Kutzner, H.; Cronin, M.
24
25
26 T.; Stephens, P. J.; Bastian, B. C. Kinase Fusions are Frequent in Spitz Tumours
27
28
29 and Spitzoid Melanomas. *Nat. Commun.* **2014**, *5*, 3116.
30
31
32
33
34 10) Le Rolle, A. F.; Klempner, S. J.; Garrett, C. R.; Seery, T.; Sanford, E. M.;
35
36
37 Balasubramanian, S.; Ross, J. S.; Stephens, P. J.; Miller, V. A.; Ali, S. M.; Chiu,
38
39
40 V. K. Identification and Characterization of RET Fusions in Advanced Colorectal
41
42
43 Cancer. *Oncotarget* **2015**, *6*, 28929-28937.
44
45
46
47
48 11) Hechtman, J. F.; Zehir, A.; Yaeger, R. D.; Wang, L.; Middha, S.; Zheng, T.;
49
50
51 Hyman, D.; Solit, D.; Arcila, M. E.; Borsu, L.; Shia, J.; Vakiani, E.; Saltz, L.;
52
53
54 Ladanyi, M. Identification of Targetable Kinase Alterations in Patients with
55
56
57
58
59
60

Colorectal Carcinoma that are Preferentially Associated with Wild Type RAS/RAF.

Mol. Cancer Res. **2016**, *14*, 296-301.

- 12) Paratala, B. S.; Chung, J. H.; Williams, C. B.; Yilmazel, B.; Petrosky, W.; Williams, K.; Schrock, A. B.; Gay, L. M.; Lee, E.; Dolfi, S. C.; Pham, K.; Lin, S.; Yao, M.; Kulkarni, A.; DiClemente, F.; Liu, C.; Rodriguez-Rodriguez, L.; Ganesan, S.; Ross, J. S.; Ali, S. M.; Leyland-Jones, B.; Hirshfield, K. M. RET Rearrangements are Actionable Alterations in Breast Cancer. *Nat. Commun.* **2018**, *9*, 4821.

- 13) Wang, K.; Russell, J. S.; McDermott, J. D.; Elvin, J. A.; Khaira, D.; Johnson, A.; Jennings, T. A.; Ali, S. M.; Murray, M.; Marshall, C.; Oldham, D. S.; Washburn, D.; Wong, S. J.; Chmielecki, J.; Yelensky, R.; Lipson, D.; Miller, V. A.; Stephens, P. J.; Serracino, H. S.; Ross, J. S.; Bowles, D. W. Profiling of 149 Salivary Duct Carcinomas, Carcinoma Ex Pleomorphic Adenomas, and Adenocarcinomas, Not Otherwise Specified Reveals Actionable Genomic Alterations. *Clin. Cancer Res.* **2016**, *22*, 6061-6068.

- 14) Klempner, S. J.; Bazhenova, L. A.; Braiteh, F. S.; Nikolinakos, P. G.; Gowen, K.; Cervantes, C. M.; Chmielecki, J.; Greenbowe, J. R.; Ross, J. S.; Stephens, P.

- J.; Miller, V. A.; Ali, S. M.; Ou, S. H. Emergence of RET Rearrangement Co-Existing with Activated EGFR Mutation in EGFR-Mutated NSCLC Patients who had Progressed on First- or Second-Generation EGFR TKI. *Lung Cancer* **2015**, *89*, 357-359.
- 15) Wells, S. A. Jr.; Pacini, F.; Robinson, B. G.; Santoro, M. Multiple Endocrine Neoplasia Type 2 and Familial Medullary Thyroid Carcinoma: an Update. *J. Clin. Endocrinol. Metab.* **2013**, *98*, 3149-3164.
- 16) Morandi, A.; Plaza-Menacho, I.; Isacke, C. M. RET in Breast Cancer: Functional and Therapeutic Implications. *Trends Mol. Med.* **2011**, *17*, 149-157.
- 17) Nguyen, M.; Miyakawa, S.; Kato, J.; Mori, T.; Arai, T.; Armanini, M.; Gelmon, K.; Yerushalmi, R.; Leung, S.; Gao, D.; Landes, G.; Haak-Frendscho, M.; Elias, K.; Simmons, A. D. Preclinical Efficacy and Safety Assessment of an Antibody-Drug Conjugate Targeting the c-RET Proto-Oncogene for Breast Carcinoma. *Clin. Cancer Res.* **2015**, *21*, 5552-5562.
- 18) Gil, Z.; Cavel, O.; Kelly, K.; Brader, P.; Rein, A.; Gao, S. P.; Carlson, D. L.; Shah, J. P.; Fong, Y.; Wong, R. J. Paracrine Regulation of Pancreatic Cancer cell Invasion by Peripheral Nerves. *J. Natl. Cancer Inst.* **2010**, *102*, 107-118.

- 19) He, S.; Chen, C. H.; Chernichenko, N.; He, S.; Bakst, R. L.; Barajas, F.; Deborde, S.; Allen, P. J.; Vakiani, E.; Yu, Z.; Wong, R. J. GFR α 1 Released by Nerves Enhances Cancer Cell Perineural Invasion through GDNF-RET Signaling. *Proc. Natl. Acad. Sci. U S A* **2014**, *111*, E2008-E2017.
- 20) De Falco, V.; Carlomagno, F.; Li, HY.; Santoro, M. The Molecular Basis for RET Tyrosine-kinase Inhibitors in Thyroid Cancer. *Best Pract. Res. Clin. Endocrinol. Metab.* **2017**, *31*, 307-318.
- 21) Drilon, A.; Hu, Z. I.; Lai, G. G. Y. Tan DSW. Targeting RET-Driven Cancers: Lessons from Evolving Preclinical and Clinical Landscapes. *Nat. Rev. Clin. Oncol.* **2018**, *15*, 151-167.
- 22) Commander, H.; Whiteside, G.; Perry, C. Vandetanib: First Global Approval. *Drugs* **2011**, *71*, 1355-1365.
- 23) Grüllich, C. Cabozantinib: a MET, RET, and VEGFR2 Tyrosine Kinase Inhibitor. *Recent Results Cancer Res.* **2014**, *201*, 207-214.
- 24) Wells, S. A. Jr.; Robinson, B. G.; Gagel, R. F.; Dralle, H.; Fagin, J. A.; Santoro, M.; Baudin, E.; Elisei, R.; Jarzab, B.; Vasselli, J. R.; Read, J.; Langmuir, P.; Ryan, A. J.; Schlumberger, M. J. Vandetanib in Patients with Locally Advanced or

Metastatic Medullary Thyroid Cancer: a Randomized, Double-Blind Phase III trial.

J. Clin. Oncol. **2012**, *30*, 134-141.

- 25) Elisei, R.; Schlumberger, M. J.; Müller, S. P.; Schöffski, P.; Brose, M. S.; Shah, M. H.; Licitra, L.; Jarzab, B.; Medvedev, V.; Kreissl, M. C.; Niederle, B.; Cohen, E. E.; Wirth, L. J.; Ali, H.; Hessel, C.; Yaron, Y.; Ball, D.; Nelkin, B.; Sherman, S. I. Cabozantinib in Progressive Medullary Thyroid Cancer. *J. Clin. Oncol.* **2013**, *31*, 3639-3646.
- 26) Schlumberger, M.; Tahara, M.; Wirth, L. J.; Robinson, B.; Brose, M. S.; Elisei, R.; Habra, M. A.; Newbold, K.; Shah, M. H.; Hoff, A. O.; Gianoukakis, A. G.; Kiyota, N.; Taylor, M. H.; Kim, S. B.; Krzyzanowska, M. K.; Dutcus, C. E.; de las Heras, B.; Zhu, J.; Sherman, S. I. Lenvatinib Versus Placebo in Radioiodine-Refractory Thyroid Cancer. *N. Engl. J. Med.* **2015**, *372*, 621-630.
- 27) White, P. T.; Cohen, M. S. The Discovery and Development of Sorafenib for the Treatment of Thyroid Cancer. *Expert Opin. Drug Discov.* **2015**, *10*, 427-439.
- 28) Subbiah, V.; Gainor, J. F.; Rahal, R.; Brubaker, J. D.; Kim, J. L.; Maynard, M.; Hu, W.; Cao, Q.; Sheets, M. P.; Wilson, D.; Wilson, K. J.; DiPietro, L.; Fleming, P.; Palmer, M.; Hu, M. I.; Wirth, L.; Brose, M. S.; Ou, S. I.; Taylor, M.; Garraalda, E.;

- Miller, S.; Wolf, B.; Lengauer, C.; Guzi, T.; Evans, E. K. Precision Targeted Therapy with BLU-667 for RET-Driven Cancers. *Cancer Discov.* **2018**, *8*, 836-849.
- 29) Subbiah, V.; Velcheti, V.; Tuch, B. B.; Ebata, K.; Busaidy, N. L.; Cabanillas, M. E.; Wirth, L. J.; Stock, S.; Smith, S.; Lauriault, V.; Corsi-Travali, S.; Henry, D.; Burkard, M.; Hamor, R.; Bouhana, K.; Winski, S.; Wallace, R. D.; Hartley, D.; Rhodes, S.; Reddy, M.; Brandhuber, B. J.; Andrews, S.; Rothenberg, S. M.; Drilon, A. Selective RET Kinase Inhibition for Patients with RET-Altered Cancers. *Ann. Oncol.* **2018**, *29*, 1869-1876.
- 30) Drilon, A.; Fu, S.; Patel, M. R.; Fakih, M.; Wang, D.; Olszanski, A. J.; Morgensztern, D.; Liu, S. V.; Cho, B. C.; Bazhenova, L.; Rodriguez, C. P.; Doebele, R. C.; Wozniak, A.; Reckamp, K. L.; Seery, T.; Nikolinakos, P.; Hu, Z.; Oliver, J. W.; Trone, D.; McArthur, K.; Patel, R.; Multani, P. S.; Ahn, M. J. A Phase I/Ib Trial of the VEGFR-Sparing Multikinase RET Inhibitor RXDX-105. *Cancer Discov.* **2019**, *9*, 384-395.
- 31) Frett, B.; Carlomagno, F.; Moccia, M. L.; Brescia, A.; Federico, G.; De Falco, V.; Admire, B.; Chen, Z.; Qi, W.; Santoro, M.; Li, H.Y. Fragment-Based Discovery

- of a Dual pan-RET/VEGFR2 Kinase Inhibitor Optimized for Single-Agent Polypharmacology. *Angew. Chem. Int. Ed. Engl.* **2015**, *54*, 8717-8721.
- 32) Yamazaki, H. Drug-Metabolizing Enzyme Systems I. In *Comprehensive Medicinal Chemistry III*; Chackalamannil, S.; Rotella, D.; Ward, S. Eds: Elsevier (Netherlands), 2017; pp 45-50.
- 33) Zhang, J.; Yang, P. L.; Gray, N. S. Targeting Cancer with Small Molecule Kinase Inhibitors. *Nat. Rev. Cancer* **2009**, *9*, 28-39.
- 34) Carlomagno, F.; Guida, T.; Anaganti, S.; Vecchio, G.; Fusco, A.; Ryan, A. J.; Billaud, M.; Santoro, M. Disease Associated Mutations at Valine 804 in the RET Receptor Tyrosine Kinase Confer Resistance to Selective Kinase Inhibitors. *Oncogene* **2004**, *23*, 6056-6063.
- 35) Mologni, L.; Redaelli, S.; Morandi, A.; Plaza-Menacho, I.; Gambacorti-Passerini, C. Ponatinib is a Potent Inhibitor of Wild-Type and Drug-Resistant Gatekeeper Mutant RET Kinase. *Mol. Cell. Endocrinol.* **2013**, *377*, 1-6.
- 36) Plenker, D.; Riedel, M.; Brägelmann, J.; Dammert, M. A.; Chauhan, R.; Knowles, P. P.; Lorenz, C.; Keul, M.; Bührmann, M.; Pagel, O.; Tischler, V.; Scheel, A. H.; Schütte, D.; Song, Y.; Stark, J.; Mrugalla, F.; Alber, Y.; Richters, A.;

- Engel, J.; Leenders, F.; Heuckmann, J. M.; Wolf, J.; Diebold, J.; Pall, G.; Peifer, M.; Aerts, M.; Gevaert, K.; Zahedi, R. P.; Buettner, R.; Shokat, K. M.; McDonald, N. Q.; Kast, S. M.; Gautschi, O.; Thomas, R. K.; Sos, M. L. Drugging the Catalytically Inactive State of RET kinase in RET-Rearranged Tumors. *Sci. Transl. Med.* **2017**, *9*, 394.
- 37) Vedadi, M.; Niesen, F. H.; Allali-Hassani, A.; Fedorov, O. Y.; Finerty, P. J. Jr.; Wasney, G. A.; Yeung, R.; Arrowsmith, C.; Ball, L. J.; Berglund, H.; Hui, R.; Marsden, B. D.; Nordlund, P.; Sundstrom, M.; Weigelt, J.; Edwards, A. M. Chemical Screening Methods to Identify Ligands that Promote Protein Stability, Protein Crystallization, and Structure Determination. *Proc. Natl. Acad. Sci. U S A* **2006**, *103*, 15835-15840.
- 38) Nakaoku, T.; Kohno, T.; Araki, M.; Niho, S.; Chauhan, R.; Knowles, P. P.; Tsuchihara, K.; Matsumoto, S.; Shimada, Y.; Mimaki, S.; Ishii, G.; Ichikawa, H.; Nagatoishi, S.; Tsumoto, K.; Okuno, Y.; Yoh, K.; McDonald, N. Q.; Goto, K. A Secondary RET Mutation in the Activation Loop Conferring Resistance to Vandetanib. *Nat. Commun.* **2018**, *9*, 625.

- 1
2
3
4 39) Bullock, A. N.; Debreczeni, J. E.; Fedorov, O. Y.; Nelson, A.; Marsden, B. D.;
5
6
7 Knapp, S. Structural Basis of Inhibitor Specificity of the Human Protooncogene
8
9
10 Proviral Insertion Site in Moloney Murine Leukemia Virus (PIM-1) Kinase. *J. Med.*
11
12
13 *Chem.* **2005**, *48*, 7604-7614.
14
15
16
17 40) Kufareva, I.; Abagyan, R. Type-II Kinase Inhibitor Docking, Screening, and
18
19
20 Profiling Using Modified Structures of Active Kinase States. *J. Med. Chem.* **2008**,
21
22
23 *51*, 7921-7932.
24
25
26
27 41) Plaza-Menacho, I.; Barnouin, K.; Goodman, K.; Martínez-Torres, R. J.; Borg,
28
29
30 A.; Murray-Rust, J.; Mouilleron, S.; Knowles, P.; McDonald, N. Q. Oncogenic RET
31
32
33 Kinase Domain Mutations Perturb the Autophosphorylation Trajectory by
34
35
36 Enhancing Substrate Presentation in Trans. *Mol. Cell* **2014**, *53*, 738-751.
37
38
39
40
41 42) Kitayama, H.; Kanakura, Y.; Furitsu, T.; Tsujimura, T.; Oritani, K.; Ikeda, H.;
42
43
44 Sugahara, H.; Mitsui, H.; Kanayama, Y.; Kitamura, Y. Constitutively Activating
45
46
47 Mutations of C-Kit Receptor Tyrosine Kinase Confer Factor-Independent Growth
48
49
50 and Tumorigenicity of Factor-Dependent Hematopoietic Cell Lines. *Blood* **1995**,
51
52
53 *85*, 790-798.
54
55
56
57
58
59
60

- 1
2
3
4 43) Yan, W.; Lakkaniga, N. R.; Carlomagno, F.; Santoro, M.; McDonald, N. Q.; Lv,
5
6
7 F.; Gunaganti, N.; Frett, B.; Li, HY. Insights into Current Tropomyosin Receptor
8
9
10 Kinase (TRK) Inhibitors: Development and Clinical Application. *J. Med. Chem.*
11
12
13
14 **2019**, *62*, 1731-1760.
15
16
17 44) Pargellis, C.; Tong, L.; Churchill, L.; Cirillo, P. F.; Gilmore, T.; Graham, A. G.;
18
19
20 Grob, P. M.; Hickey, E. R.; Moss, N.; Pav, S.; Regan, J. Inhibition of p38 MAP
21
22
23 Kinase by Utilizing a Novel Allosteric Binding Site. *Nat. Struct. Biol.* **2002**, *9*, 268-
24
25
26
27 272.
28
29
30 45) Knowles, P. P.; Murray-Rust, J.; Kjaer, S.; Scott, R. P.; Hanrahan, S.; Santoro,
31
32
33 M.; Ibáñez, C. F.; McDonald, N. Q. Structure and Chemical Inhibition of the RET
34
35
36 Tyrosine Kinase Domain. *J. Biol. Chem.* **2006**, *281*, 33577-33587.
37
38
39
40 46) Pasini, A.; Geneste, O.; Legrand, P.; Schlumberger, M.; Rossel, M.;
41
42
43
44 Fournier, L.; Rudkin, B. B.; Schuffenecker, I.; Lenoir, G. M.; Billaud, M. Oncogenic
45
46
47 Activation of RET by Two Distinct FMTC Mutations Affecting the Tyrosine Kinase
48
49
50
51 Domain. *Oncogene* **1997**, *15*, 393-402.
52
53
54
55
56
57
58
59
60

- 1
2
3
4 47) Ishizaka, Y.; Ushijima, T.; Sugimura, T.; Nagao, M. cDNA Cloning and
5
6
7 Characterization of Ret Activated in a Human Papillary Thyroid Carcinoma Cell
8
9
10 Line. *Biochem. Biophys. Res. Commun.* **1990**, *168*, 402-408.
11
12
13
14 48) Carlomagno, F.; Salvatore, D.; Santoro, M.; de Franciscis, V.; Quadro, L.;
15
16
17 Panariello, L.; Colantuoni, V.; Fusco, A. Point Mutation of the RET Proto-
18
19
20 Oncogene in the TT Human Medullary Thyroid Carcinoma Cell Line. *Biochem.*
21
22
23
24 *Biophys. Res. Commun.* **1995**, *207*, 1022–1028.
25
26
27
28 49) Suzuki, M.; Makinoshima, H.; Matsumoto, S.; Suzuki, A.; Mimaki, S.;
29
30
31 Matsushima, K.; Yoh, K.; Goto, K.; Suzuki, Y.; Ishii, G.; Ochiai, A.; Tsuta, K.;
32
33
34 Shibata, T.; Kohno T, Esumi, H.; Tsuchihara, K. Identification of a Lung
35
36
37 Adenocarcinoma Cell Line with CCDC6-RET Fusion Gene and the Effect of RET
38
39
40 Inhibitors in Vitro and in Vivo. *Cancer Sci.* **2013**, *104*, 896-903.
41
42
43
44
45 50) Carlomagno, F.; Vitagliano, D.; Guida, T.; Basolo, F.; Castellone, M. D.; Melillo,
46
47
48 R. M.; Fusco, A.; Santoro, M. Efficient Inhibition of RET/Papillary Thyroid
49
50
51 Carcinoma Oncogenic Kinases by 4-amino-5-(4-chloro-phenyl)-7-(t-
52
53
54 butyl)pyrazolo[3,4-d]pyrimidine (PP2). *J. Clin. Endocrinol. Metab.* **2003**, *88*, 1897-
55
56
57
58
59 1902.
60

FIGURES and LEGENDS

Fig. 1

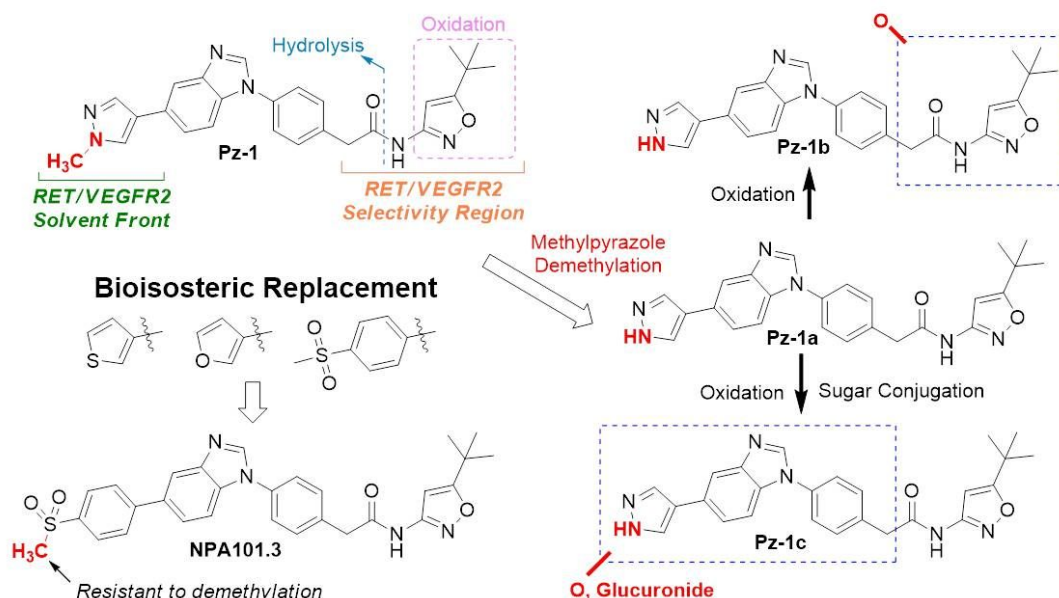


Figure 1: Metabolism of Pz-1 and Bioisosteric Replacement Methods — Pz-1 is hydrolyzed, oxidized, or demethylated via Phase 1 metabolic systems. Hydrolysis and oxidation occur in the selectivity region for binding to RET and VEGFR2, while demethylation occurs at the solvent front for both kinases. Bioisosteric replacement at the solvent front was performed by replacing methylpyrazole with (methylsulfonyl)benzene, generating NPA101.3. VEGFR2 DFG-out crystal structure (PDB# 2OH4);

1
2
3
4
5
6
7
8
9
10
11
12
13
14
15
16
17
18
19
20
21
22
23
24
25
26
27
28
29
30
31
32
33
34
35
36
37
38
39
40
41
42
43
44
45
46
47
48
49
50
51
52
53
54
55
56
57
58
59
60

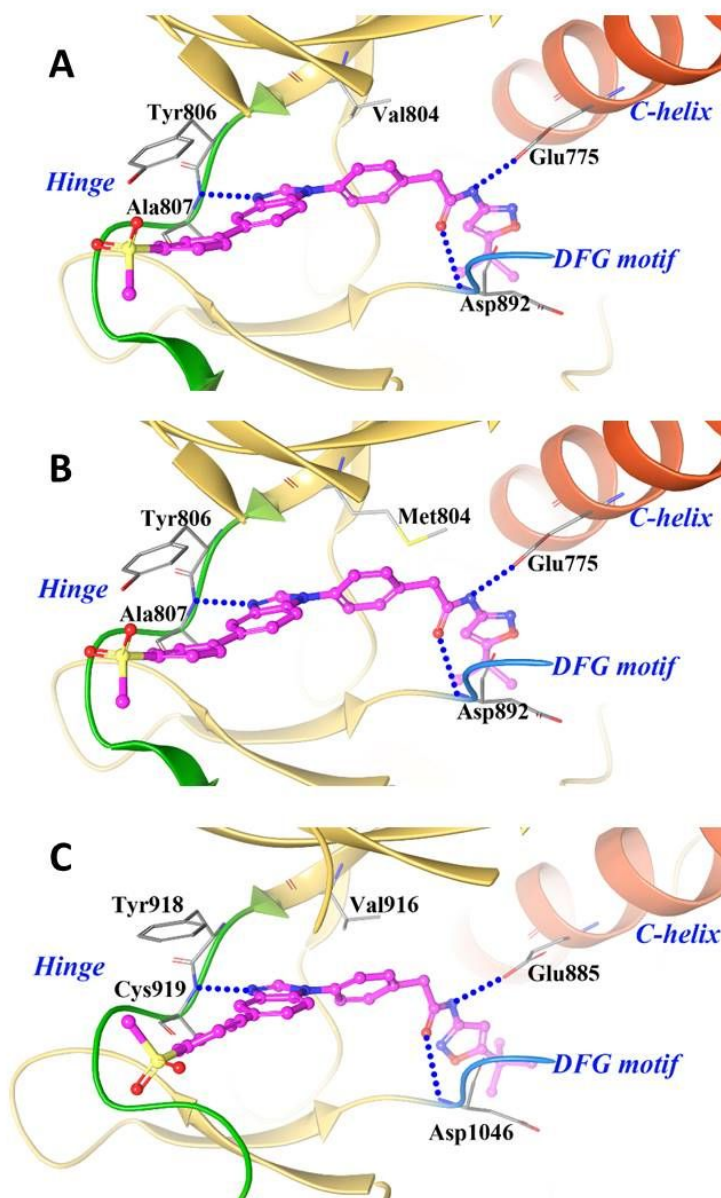
Fig. 2

Figure 2: Computational modelling of NPA101.3 — (A) NPA101.3 computationally modelled in a RET DFG-out homology model. The model shows the hydrogen bond at the ATP binding site with A807, a hydrogen bond network at the DFG motif, and interaction with Y806 via π - π stacking. The model also shows that *p*-sulfone of NPA101.3 is solvent exposed. Hydrogen bonds are shown with blue dotted lines. (B) NPA101.3 computationally modelled in a RET/V804M DFG-out homology model. NPA101.3 is able to accommodate bulky mutations at the gatekeeper residue. (C)

1
2
3 NPA101.3 computationally modelled in the VEGFR2 kinase. The binding mode is
4
5
6 near identical to the binding in RET, with exception of the isoxazole orientation in the
7
8
9 allosteric pocket. Flexibility at the methylene linker is predicted to permit the balanced
10
11 affinity of NPA101.3 to RET and VEGFR2.
12
13
14
15
16
17
18
19
20
21
22
23
24
25
26
27
28
29
30
31
32
33
34
35
36
37
38
39
40
41
42
43
44
45
46
47
48
49
50
51
52
53
54
55
56
57
58
59
60

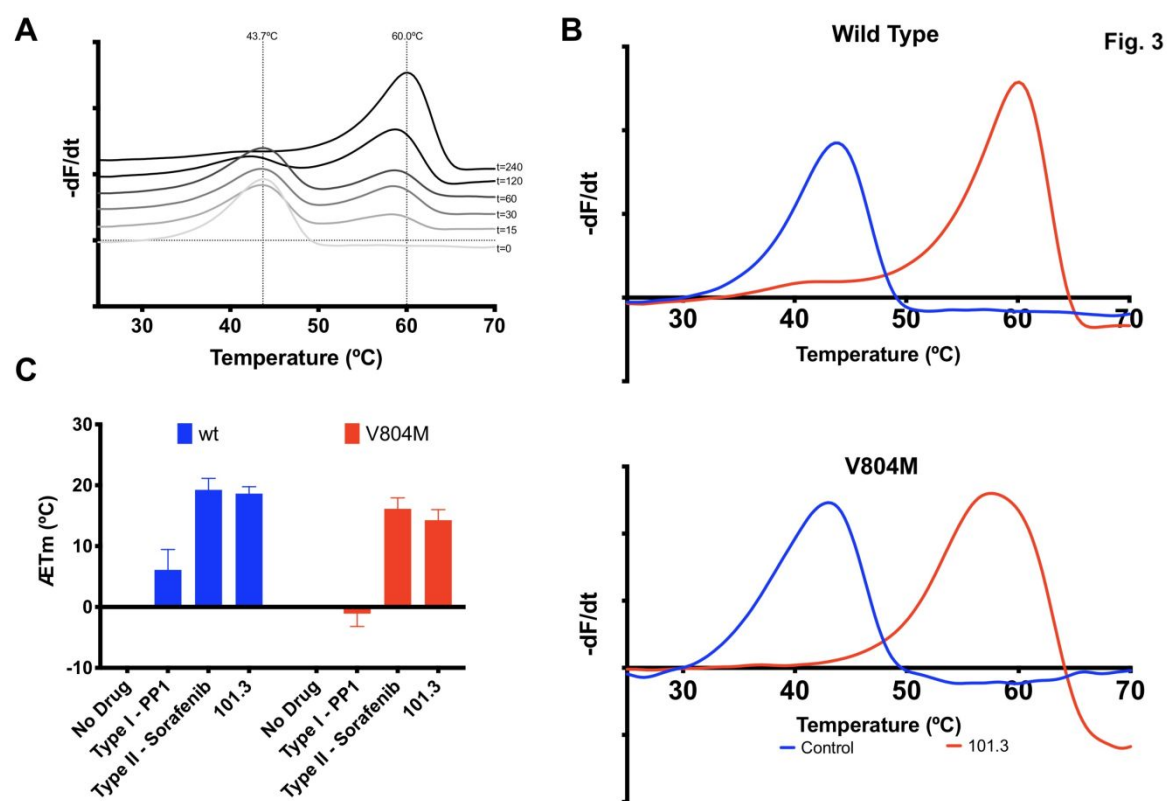


Figure 3: Thermal shift assay determination of the type-2 binding mode of NPA101.3

— (A) Representative experiment of binding of NPA101.3 to wild type RET core kinase domain monitored by the change in thermal stability. The melting temperature T_m is obtained from the first derivative of the change in fluorescence ($-dF/dt$) taken from the top of the peak in the derivative plot. (B) Plot of the derivative of the change in fluorescence ($-dF/dt$) for the wild type protein or V804M mutant in the presence of NPA101.3 or buffer for a representative experiment. The compound binds equally well to either RET protein (C) Tabulated average melting temperature differences (ΔT_m) from four independent experiments after addition of NPA101.3, PP1 (a known

1
2
3 type-1 inhibitor) or Sorafenib (a known type-2 inhibitor). The respective SD errors are
4
5
6 shown for each drug.
7
8
9
10
11
12
13
14
15
16
17
18
19
20
21
22
23
24
25
26
27
28
29
30
31
32
33
34
35
36
37
38
39
40
41
42
43
44
45
46
47
48
49
50
51
52
53
54
55
56
57
58
59
60

Fig. 4

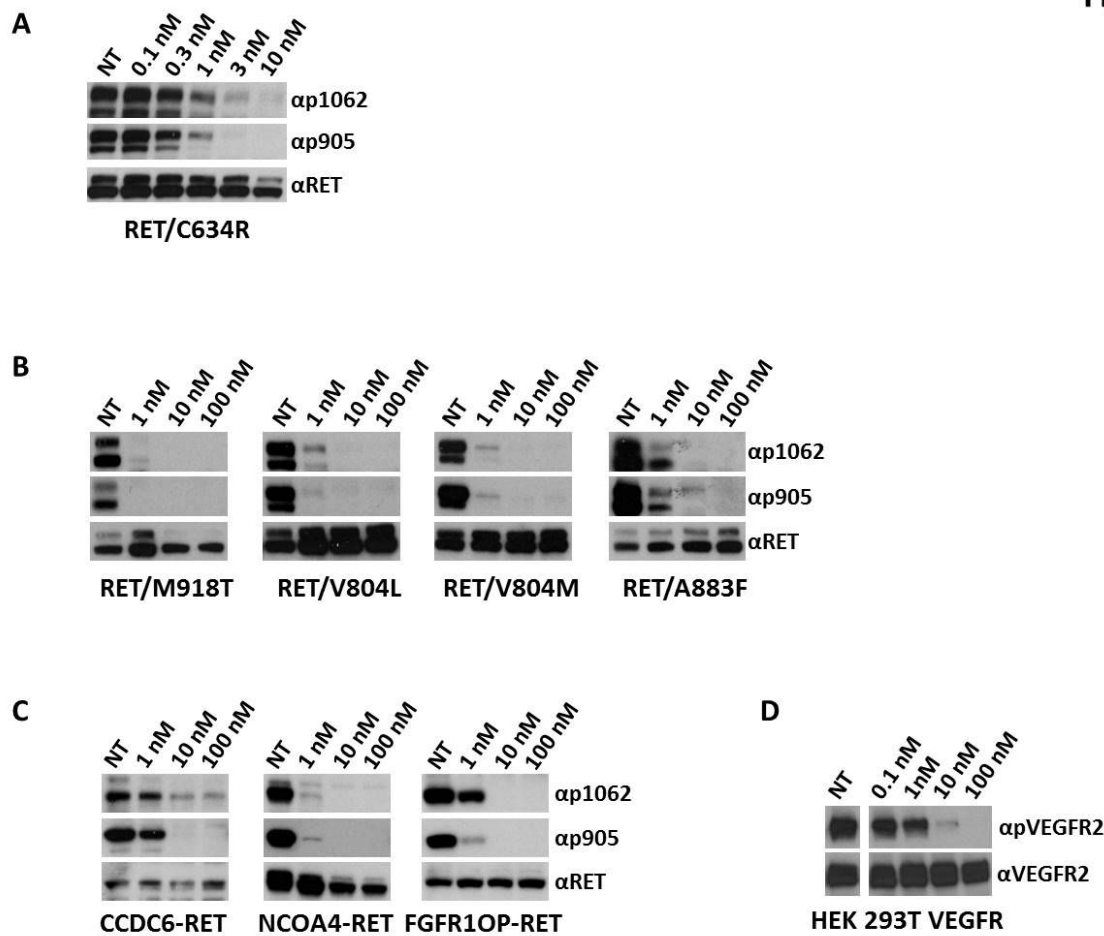


Figure 4: NPA101.3-mediated inhibition of phosphorylation and signalling of oncogenic RET mutants and VEGFR2 in intact cells — Serum-starved RAT1 cells exogenously expressing the indicated RET point mutants (A, B) or NIH3T3 cells exogenously expressing the indicated RET rearranged mutants (C) were treated for 2 hr with indicated concentrations of compound. Total cell lysates (50 μ g) were subjected to immunoblotting with anti-phospho-Y1062 (α p1062) and anti-phospho-Y905 (α p905) RET antibodies. The blots were normalized using anti-RET (α RET) antibody. D) HEK293 cells were transiently transfected with human VEGFR2; 36 hr

1
2
3 after transfection, cells were serum starved for 12 hr. The indicated doses of
4
5
6 compound or vehicle (NT) were added for 2 hr and then VEGFA (100 ng/ml)
7
8
9 stimulation was applied for 15 min. Cell lysates were immunoblotted with anti-
10
11 phospho-VEGFR2 (α pVEGFR2) antibody. The blot was normalized using anti-
12
13 VEGFR2 (α VEGFR2) antibody.
14
15
16
17
18
19
20
21
22
23
24
25
26
27
28
29
30
31
32
33
34
35
36
37
38
39
40
41
42
43
44
45
46
47
48
49
50
51
52
53
54
55
56
57
58
59
60

Fig. 5

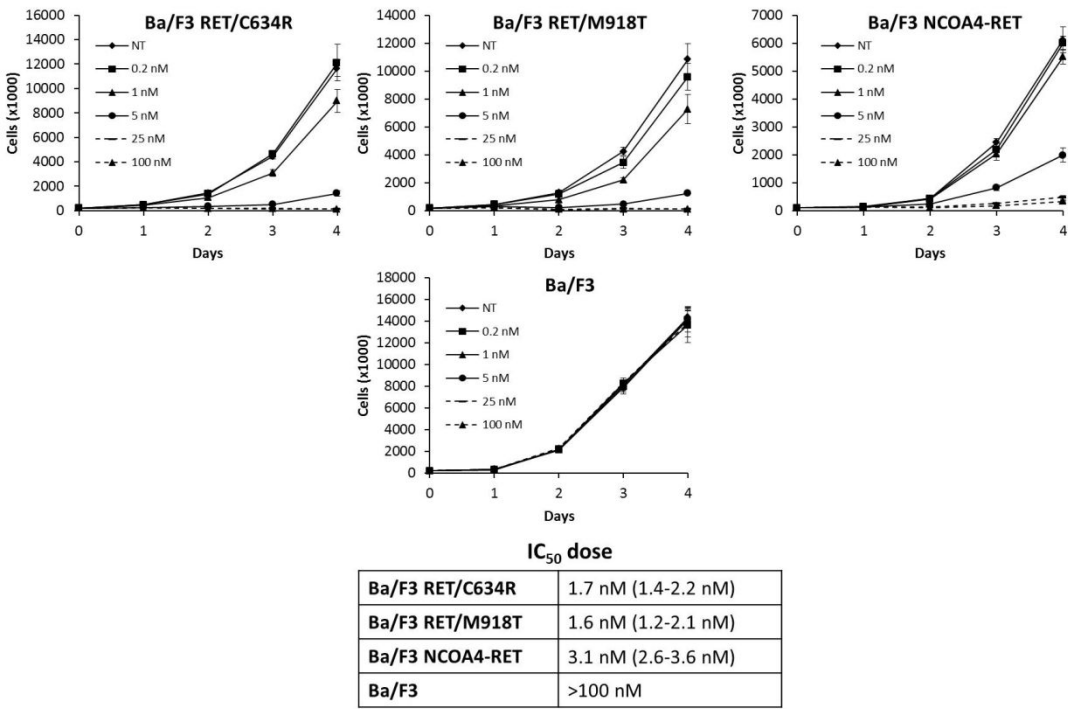


Figure 5: NPA101.3-mediated inhibition of proliferation of RET-transformed Ba/F3 cells — Parental and RET/C634R, RET M918T and NCOA4-RET transfected Ba/F3 cells were incubated with vehicle (NT: not treated) or the indicated concentrations of NPA101.3 and counted at the indicated time points. Parental cells were supplemented with IL3 (10 ng/ml). Data are the mean \pm SD of a single experiment performed in triplicate. Growth inhibition IC₅₀ doses of the compound for the different cell lines are reported. 95% CI are indicated in brackets.

Fig. 6

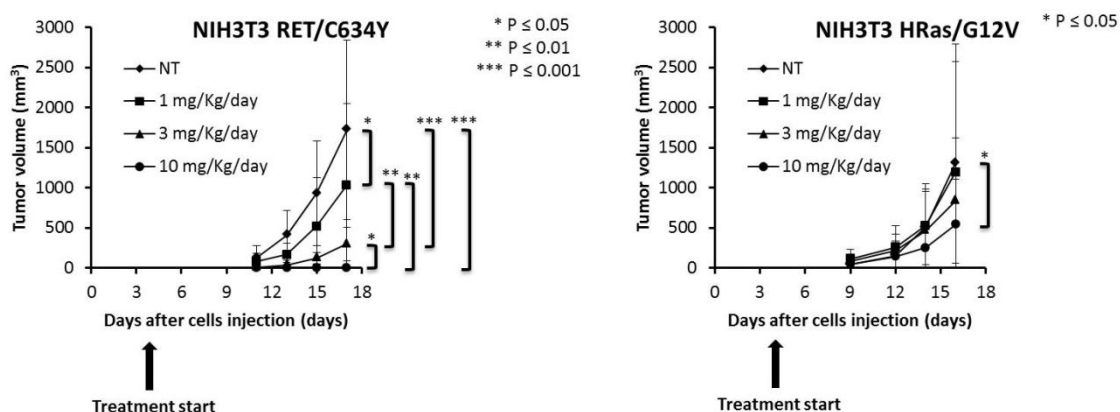
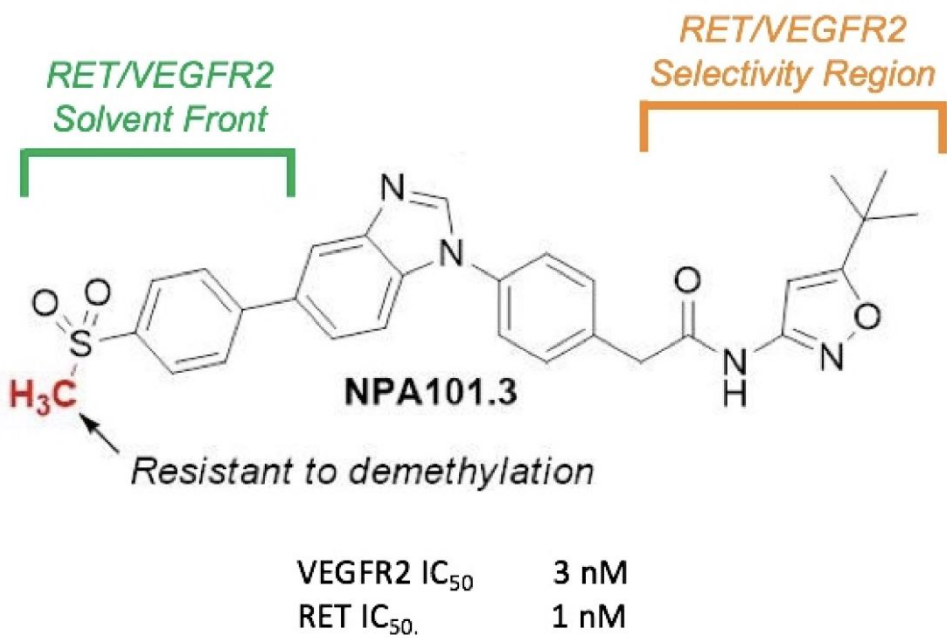


Figure 6: Effects of NPA101.3 on *in vivo* tumour growth — NIH3T3 cells transformed by RET/C634Y or HRAS/G12V were inoculated subcutaneously into nu/nu mice. After 4 days, animals were randomly assigned to receive for the indicated time periods the compound (1.0, 3.0 or 10 mg/kg daily) (24 mice: 8 mice/group for 1, 3 and 10 mg/kg doses) or vehicle (8 mice) by oral gavage. Average size of tumors is reported \pm SD.

Table of Contents graphic



**Bioisosteric discovery of NPA101.3, a second generation pan-RET/VEGFR2
inhibitor, optimized for single-agent polypharmacology**

Supporting Information

Marialuisa Moccia, Brendan Frett et al.

Supplementary Methods

RET DFG-out Homology Model Development. A VEGFR2 DFG-out crystal structure (PDB# 2OH4) and the amino acid sequence of RET (PDB# 2IVU) were obtained. Using SWISS-MODEL Automatic Modelling Mode (swissmodel.expasy.org), the RET sequence was employed to build a RET DFG-out homology model using the VEGFR2 DFG-out structure as a template. The resulting RET DFG-out homology model was used to complete molecular modeling studies. The RET DFG-out homology model is available in the Supplemental Information.

Molecular modelling. Using AutoDock Tools, all hydrogens were added as 'Polar Only' and a grid box for the ATP binding site was created (center x = -25.881, center y = 9.55, center z = -10.927 / size x = 16, size y = 44, size z = 18) in the RET DFG-out homology model. Compounds to be computationally modelled were assigned appropriate rotatable bonds using AutoDock Tools. AutoDock Vina was employed to computationally model the compounds. AutoDock Vina reports receptor affinity in terms of ΔG of the receptor/ligand complex. The modelling results were visualized and analysed with Discovery Studio 3.5.

Kinome scan. NPA101.3 (100 nM) was subjected to a kinome scan against a 96 kinases panel representing major kinome clusters. The screening (KINOMEscan) was outsourced to DiscoverX (Fremont, CA, United States)

Synthesis of ethyl 2-(4-((4-bromo-2-nitrophenyl)amino)phenyl)acetate (1a). Ethyl 4-aminophenyl acetate (3.67 g, 20.45 mmol) was added to a 20 mL microwave vial along with 4-bromo-1-fluoro-2-nitrobenzene (3.00 g, 13.64 mmol) and DMA (10 mL). The reaction was sealed and placed under microwave irradiation for 30 minutes at 160 °C. The crude reaction was added to water and extracted with EtOAc. The organic extract was washed with brine 1X, acidified water (pH ~4) 2X, and brine 2X. The organic layer was collected, dried with MgSO_4 , and adsorbed on silica. The reaction was purified using flash chromatography with hexanes/EtOAc to afford **1a** as blood-red oil that eventually solidified (4.2 g, 81%). ^1H NMR (400 MHz, Chloroform-

d) δ 9.41 (s, 1H), 8.34 (d, J = 2.4 Hz, 1H), 7.41 (ddd, J = 9.2, 2.4, 0.6 Hz, 1H), 7.34 (d, J = 8.3 Hz, 2H), 7.21 (d, J = 8.3 Hz, 2H), 7.10 (d, J = 9.2 Hz, 1H), 4.18 (q, J = 7.2 Hz, 2H), 3.63 (s, 2H), 1.28 (t, J = 7.2 Hz, 3H). ESIMS m/z [M+H]⁺ 379.

Synthesis of ethyl 2-(4-((2-amino-4-bromophenyl)amino)phenyl)acetate (1b).

Compound **1a** (2.03 g, 5.35 mmol) was placed into a 250 mL round bottom flask. EtOH (80 mL) and zinc (2.450 g, 37.5 mmol) were added to the flask and the reaction was placed in an ice bath. Acetic acid (2.145 mL, 37.5 mmol) diluted with EtOH (40 mL) was added dropwise to the reaction over the course of 1 hour. After the addition, the reaction was stirred at 0 °C for 5 hours. The reaction was filtered and EtOH was evaporated. The reaction was slowly basified with aqueous NaHCO₃ and extracted with diethyl ether. The reaction was washed 3X with aqueous NaHCO₃ and the organic layer was collected, dried with MgSO₄, and evaporated to yield **1b** as a slight purple solid (1.834 g, 98%). ¹H NMR (400 MHz, Chloroform-*d*) δ 7.12 (d, J = 8.5 Hz, 2H), 6.95 (d, J = 8.3 Hz, 1H), 6.92 (d, J = 2.2 Hz, 1H), 6.83 (dd, J = 8.3, 2.2 Hz, 1H), 6.67 (d, J = 8.5 Hz, 2H), 5.07 (s, 1H), 4.14 (q, J = 7.1 Hz, 2H), 3.82 (s, 2H), 3.51 (s, 2H), 1.25 (t, J = 7.1 Hz, 3H). ESIMS m/z [M+H]⁺ 349.

Synthesis of ethyl 2-(4-(5-bromo-1H-benzo[d]imidazol-1-yl)phenyl)acetate (1).

Compound **1b** (2.01 g, 5.76 mmol) was added to a 150 mL round bottom flask followed by TMOF (50 mL) and a stir bar. After, pTSA (59.6 mg, 0.314 mmol) was added and the reaction was stirred at room temperature for about an hour or until complete conversion based on TLC. After complete consumption of the starting material, the reaction was extracted with EtOAc and washed with NaHCO₃ 3X and brine 3X. The organic layer was collected, dried with MgSO₄, and condensed to yield **1** as a brown solid (2.04 g, 99%). ¹H NMR (400 MHz, Chloroform-*d*) δ 8.08 (s, 1H), 8.02 (dd, J = 1.7, 0.6 Hz, 1H), 7.51 (d, J = 8.7 Hz, 2H), 7.47 – 7.42 (m, 3H), 7.39 (dd, J = 8.7, 0.6 Hz, 1H), 4.21 (q, J = 7.1 Hz, 2H), 3.72 (s, 2H), 1.30 (t, J = 7.1 Hz, 3H). ESIMS m/z [M+H]⁺ 359.

Synthesis of N-(5-(tert-butyl)isoxazol-3-yl)-2-(4-(5-(4-(methylsulfonyl)phenyl)-1H-benzo[d]imidazol-1-yl)phenyl)acetamide (NPA-101.3). Compound **1** (150 mg, 0.418 mmol) was placed into a 20 mL microwave vial along with 4:1 DMF/Water (5 mL). (4-

(methylsulfonyl)phenyl)boronic acid (109 mg, 0.543 mmol) was added to the vial along with Na_2CO_3 (175 mg, 1.670 mmol). The reaction vessel was degassed with N_2 for 10 minutes, followed by the addition of $\text{Pd}(\text{dppf})\text{Cl}_2$ (1.169 mg, 0.004 mmol). The reaction vessel was sealed under N_2 and microwaved at 130 °C for 20 minutes. After, upon solvent evaporation, the crude product was dissolved in DCM and washed with NaHCO_3 3X and brine 3X. The organic layer was collected, dried with MgSO_4 , and condensed to yield crude product (120 mg). The crude product was dissolved in 1:1 THF/Water (4 mL). LiOH (26.5 mg, 1.105 mmol) was added to the reaction and the reaction was heated under microwave irradiation for 10 minutes at 100 °C. The reaction was subsequently acidified to a pH of ~3-4 and extracted 5X with 4:1 chloroform/IPA. The organic layer was dried with MgSO_4 and condensed to yield the acid (90.7 mg). The acid was added to a 5 mL vial. Anhydrous DMF (3 mL) was added to the vial, followed by EDC (52.5 mg, 0.338 mmol) and DMAP (8.10 mg, 0.0066 mmol). 5-(tert-butyl)isoxazol-3-amine (40.4 mg, 0.288 mmol) was added and the reaction was sealed under N_2 and was stirred at room temperature for 12 hours. The reaction was quenched with water, extracted with 4:1 chloroform/IPA, and washed with saturated NaHCO_3 5X. The organic layer was collected, dried with MgSO_4 , adsorbed onto silica, and purified by flash chromatography using a DCM/MeOH to generate NPA-101.3 (2) (39.7 mg, 18.0%). ^1H NMR (400 MHz, $\text{DMSO}-d_6$) δ 11.29 (s, 1H), 8.63 (s, 1H), 8.17 (s, 1H), 8.08 – 7.91 (m, 5H), 7.72 (s, 2H), 7.67 (d, J = 8.5 Hz, 2H), 7.56 (d, J = 8.5 Hz, 2H), 3.78 (s, 2H), 3.25 (s, 3H), 1.26 (s, 9H). ^{13}C NMR (101 MHz, $\text{DMSO}-d_6$) δ 144.97, 128.15, 128.08, 124.04, 123.40, 119.09, 111.86, 93.54, 44.06, 32.95, 28.76, 128.25, 180.96, 169.61, 158.35, 146.00, 131.28, 145.07, 139.49, 135.56, 134.89, 133.84, 133.60. ESIMS m/z $[\text{M}+\text{H}]^+$ 529. LC-MS Purity, >95%.

Patch-Clamp assay. The patch-clamp assay has been outsourced to Aptuit (Verona, Italy). Briefly, HEK293 cells expressing an inducible hERG were kept in cryogenic storage. After thawing, cells were maintained in culture using minimum essential medium supplemented with 10% foetal bovine serum, 1% non-essential amino acids, 1% sodium pyruvate, 2mM L-glutamine, 1% pen-strep, 15 $\mu\text{g}/\text{ml}$ blasticidin and 100 $\mu\text{g}/\text{ml}$ hygromycin. hERG channel expression induction was obtained by adding 10 $\mu\text{g}/\text{ml}$ tetracycline 48 h before the experiment. For the assay, cells were washed with extracellular solution, treated with vehicle followed by 0.1-1-10 μM concentration of NPA101.3, by positive control E-4031 or vehicle, and finally washed with extracellular solution. Current amplitude was measured and IC_{50} was calculated.

1
2
3 **LCMS plasma analysis.** NPA101.3 (10 mg/kg) was orally dosed to mice. Blood plasma
4 samples were collected at 1h and 4h after administration and analyzed by liquid
5 chromatography–mass spectrometry (LC-MS) (Thermo Surveyor LCMS System with
6 Thermo Finnigan LCQ Deca) equipped with a Phenomenex Kinetex XB-C18 column (50 x
7 2.10 mm, 5 μ m). A 5-minute gradient elution method using water and methanol (0.1% of
8 formic acid was added in both solvents) was applied. The ratio of methanol increased from
9 30% to 100% in 4 minutes and returned to 30% for column equilibration.
10
11

12 **Toxicity.** NPA101.3 (10 mg/kg) was orally dosed to 4 mice for 7 days; mice (n.4) treated with
13 vehicle alone were used as controls. Plasma was subjected to biochemical analysis. Alkaline
14 Phosphatase, Glucose, Alanine Transaminase, Total Proteins, Albumin, Globulins, Calcium,
15 Blood Urea Nitrogen (BUN) and Phosphorus were measured by using automated biochemical
16 analyzer Biotechnica Instrument BT1500 including proper calibration and QC. In particular,
17 the following methods were used: IFCC for Alkaline Phosphatase and Alanine Transaminase,
18 GOD-POD for Glucose, Buriel for Total Proteins, Bromocresol Green for Albumin, Arsenazo
19 III for Calcium, UV for Urea/BUN and Phosphorus. Globulin was: Total proteins minus
20 Albumin. The analysis was outsourced to Biogem Scarl, Ariano Irpino (AV), Italy.
21
22
23
24
25
26
27
28
29
30
31
32
33
34
35
36
37
38
39
40
41
42
43
44
45
46
47
48
49
50
51
52
53
54
55
56
57
58
59
60

1
2
3
4
5
6
7
8
9
10
11
12
13
14
15
16
17
18
19
20
21
22
23
24
25
26
27
28
29
30
31
32
33
34
35
36
37
38
39
40
41
42
43
44
45
46
47
48
49
50
51
52
53
54
55
56
57
58
59
60

Supplementary Tables

Supplementary Table S1: ΔG values of NPA101.3 in the RET DFG-out Homology Model with various (Valine 804) Gatekeeper Mutations

Protein	NPA101.3
RET Wild Type	-11.9 kcal/mol
RET V804M	-9.9 kcal/mol
RET V804L	-10.5 kcal/mol

Supplementary Table S2: NPA101.3 KinomeScan Panel screen.

NPA101.3 was screened at a single concentration of 100 nM. Hits values lower than 10% of control were considered strongly positive.

DiscoverX Symbol	Gene	Entrez Symbol	Gene	Percent Control	Compound Concentration (nM)
ACVR1		ACVR1		92	100
AKT1		AKT1		100	100
ALK		ALK		93	100
ASK1		MAP3K5		95	100
AURKA		AURKA		100	100
AURKB		AURKB		49	100
AXL		AXL		62	100
BMX		BMX		94	100
BRAF		BRAF		98	100
BRSK2		BRSK2		100	100
BTK		BTK		93	100
BUB1		BUB1		100	100
CAMK1		CAMK1		95	100
CAMK2A		CAMK2A		98	100
CDK5		CDK5		97	100
CDK7		CDK7		28	100
CDK9		CDK9		100	100
CHEK2		CHEK2		79	100
CLK1		CLK1		82	100
CSF1R		CSF1R		0.05	100
CSNK1A1		CSNK1A1		69	100
CTK		MATK		56	100
DLK		MAP3K12		100	100
DMPK		DMPK		99	100
DRAK1		STK17A		75	100
DYRK1A		DYRK1A		95	100
EGFR		EGFR		96	100
EIF2AK1		EIF2AK1		99	100
EPHA1		EPHA1		39	100
ERK1		MAPK3		100	100
FAK		PTK2		86	100

1
2
3
4
5
6
7
8
9
10
11
12
13
14
15
16
17
18
19
20
21
22
23
24
25
26
27
28
29
30
31
32
33
34
35
36
37
38
39
40
41
42
43
44
45
46
47
48
49
50
51
52
53
54
55
56
57
58
59
60

FER	FER	96	100
FGFR3	FGFR3	100	100
FRK	FRK	1.1	100
FYN	FYN	27	100
GAK	GAK	42	100
GSK3B	GSK3B	100	100
HCK	HCK	6.5	100
HIPK2	HIPK2	98	100
IGF1R	IGF1R	100	100
IKK-beta	IKBKB	100	100
INSR	INSR	100	100
IRAK4	IRAK4	100	100
ITK	ITK	72	100
JAK1(JH2domain- pseudokinase)	JAK1	93	100
JAK2(JH1domain- catalytic)	JAK2	100	100
JNK2	MAPK9	78	100
LIMK2	LIMK2	94	100
LKB1	STK11	81	100
LRRK2	LRRK2	100	100
LTK	LTK	61	100
LYN	LYN	2.8	100
MAP4K3	MAP4K3	95	100
MEK1	MAP2K1	92	100
MELK	MELK	83	100
MET	MET	79	100
MKNK2	MKNK2	0.15	100
MLK2	MAP3K10	100	100
MLK3	MAP3K11	100	100
MTOR	MTOR	97	100
MUSK	MUSK	23	100
MYLK4	MYLK4	89	100
MYO3A	MYO3A	77	100
NDR1	STK38	86	100
NEK2	NEK2	100	100
PAK1	PAK1	100	100
PCTK1	CDK16	89	100
PDPK1	PDPK1	96	100

PIK3C2B	PIK3C2B	100	100
PIK3CA	PIK3CA	100	100
PIM1	PIM1	94	100
PIM2	PIM2	94	100
PKAC-beta	PRKACB	82	100
PLK1	PLK1	99	100
PLK4	PLK4	100	100
PRKD2	PRKD2	100	100
PYK2	PTK2B	95	100
RIPK4	RIPK4	100	100
ROCK2	ROCK2	100	100
RPS6KA4(Kin.Dom.2-C-terminal)	RPS6KA4	100	100
S6K1	RPS6KB1	100	100
SLK	SLK	35	100
STK33	STK33	83	100
SYK	SYK	100	100
TAK1	MAP3K7	13	100
TIE2	TEK	30	100
TLK1	TLK1	100	100
TRKA	NTRK1	1.3	100
TRKC	NTRK3	0.25	100
TSSK1B	TSSK1B	96	100
TTK	TTK	66	100
TXK	TXK	85	100
ULK1	ULK1	100	100
ULK2	ULK2	100	100
WNK1	WNK1	93	100
YANK2	STK32B	98	100

1
2
3
4
5
6
7
8
9
10
11
12
13
14
15
16
17
18
19
20
21
22
23
24
25
26
27
28
29
30
31
32
33
34
35
36
37
38
39
40
41
42
43
44
45
46
47
48
49
50
51
52
53
54
55
56
57
58
59
60

Supplementary Table S3: NPA101.3 inhibition of hERG.

NPA101.3 was tested in a patch-clamp assay to evaluate percentage of hERG inhibition at 0.1, 1 and 10 μM with respect to vehicle. IC_{50} dose is reported

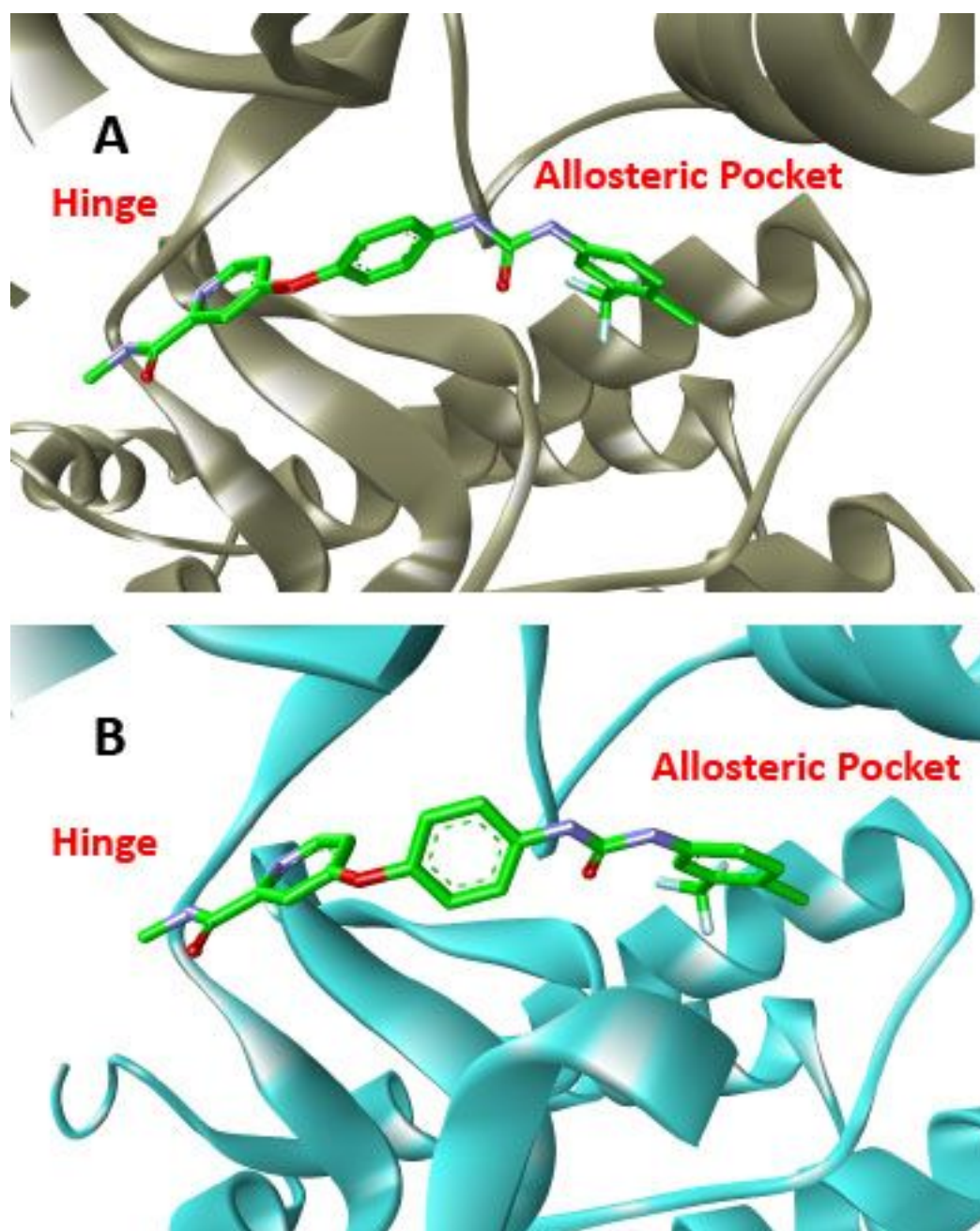
	% Mean Inhibition			IC_{50} (μM)
NPA101.3	0.1 μM	1 μM	10 μM	7.57
	0.41	14.55	55.94	
E-4031	0.003 μM	0.03 μM	0.3 μM	0.027
	2.35	53.90	93.36	

Supplementary Table S4: NPA101.3 growth inhibitory effect on human cells.

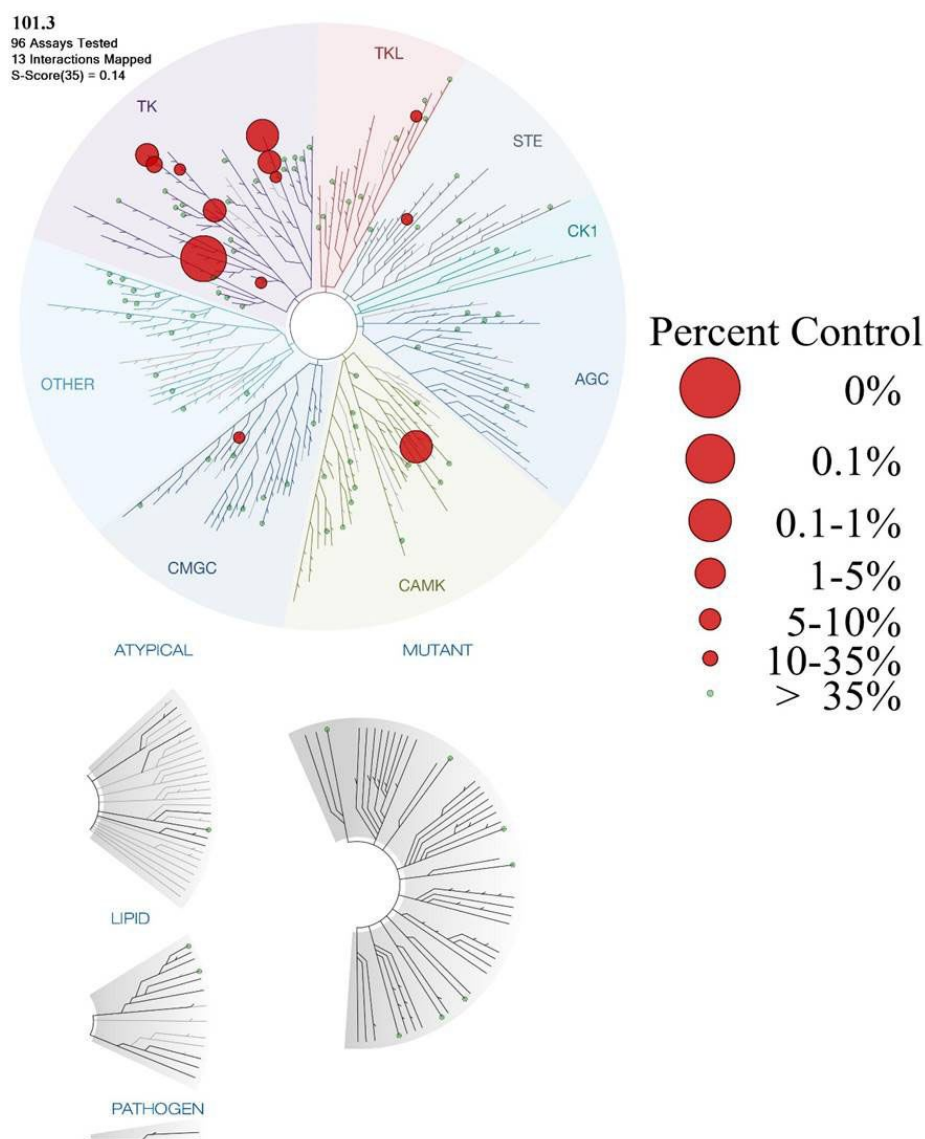
Cell line	Origin*	Oncogene mutation	IC ₅₀ nM (95% CI)
TT	MTC	RET C634W	2.19 (1.79-2.68)
MZ-CRC-1	MTC	RET M918T	2.21(1.19-4.1)
TPC-1	PTC	CCDC6-RET	0.67 (0.03-132)
Nthy-ori-3-1	thyroid	SV40 LT	> 100
BCPAP	PTC	BRAF V600E	> 100
8505-C	ATC	BRAF V600E	> 100
Lc-2/ad	LADC	CCDC6-RET	3.6 (0.9-13.9)
CALU-1	LADC	KRAS G12C	> 100
A549	LADC	KRAS G12S	> 100
PC-9	LADC	HER1 delLREA(747-750)	> 100

*MTC (medullary thyroid carcinoma); PTC (papillary thyroid carcinoma); ATC (anaplastic thyroid carcinoma); LADC (lung adenocarcinoma)

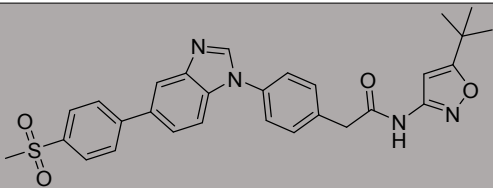
Supplementary Figures



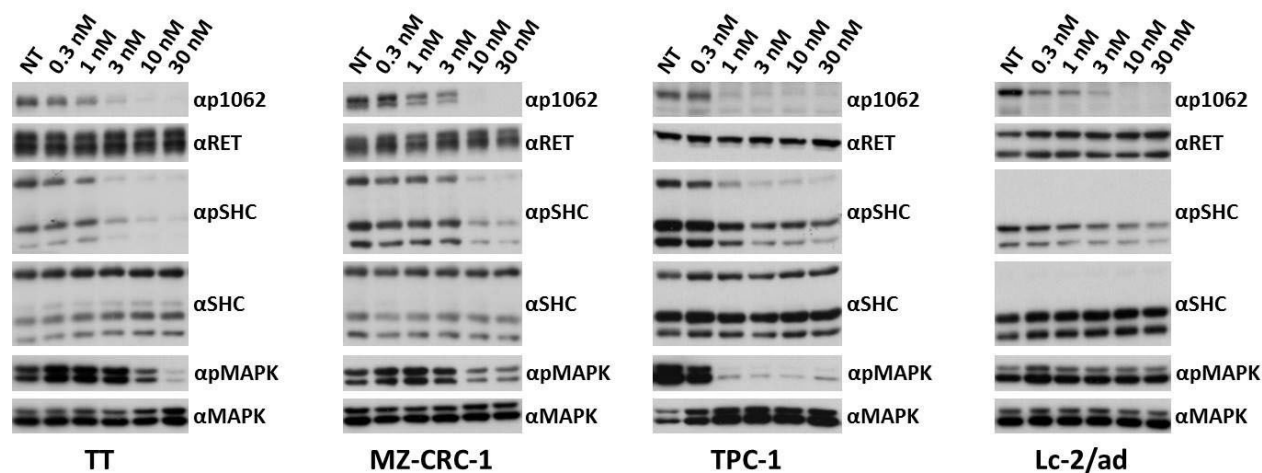
Supplementary Figure S1: Docking pose of sorafenib in the RET DFG-out model compared to X-Ray crystal structure of Sorafenib in VEGFR2 (PDB #3WZE) — Sorafenib binds to the RET DFG-out homology model (A) in a very similar pose to that of the VEGFR2 structure (B). The pose is also similar to NPA101.3 (Fig. 2), which further suggests NPA101.3 as a Type-II RET inhibitor.



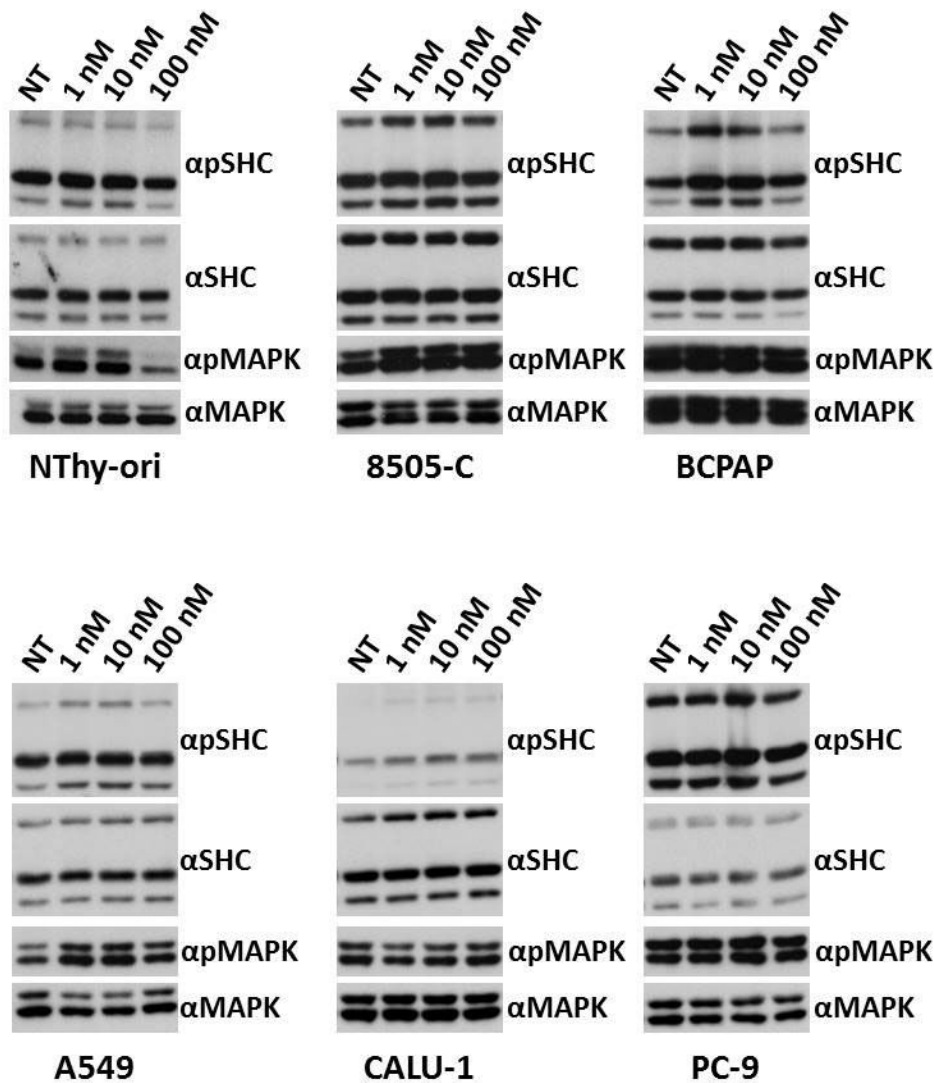
Supplementary Figure S2: NPA101.3 binding selectivity — NPA101.3 was screened against a panel of 96 kinases at a concentration of 100 nM. RET and VEGFR2 were not included in the screen because NPA101.3 inhibition of both was previously determined.

	
Kinase	NPA 101.3 IC ₅₀ (nM)
CSF1R	46
TRKA	32
RET	1

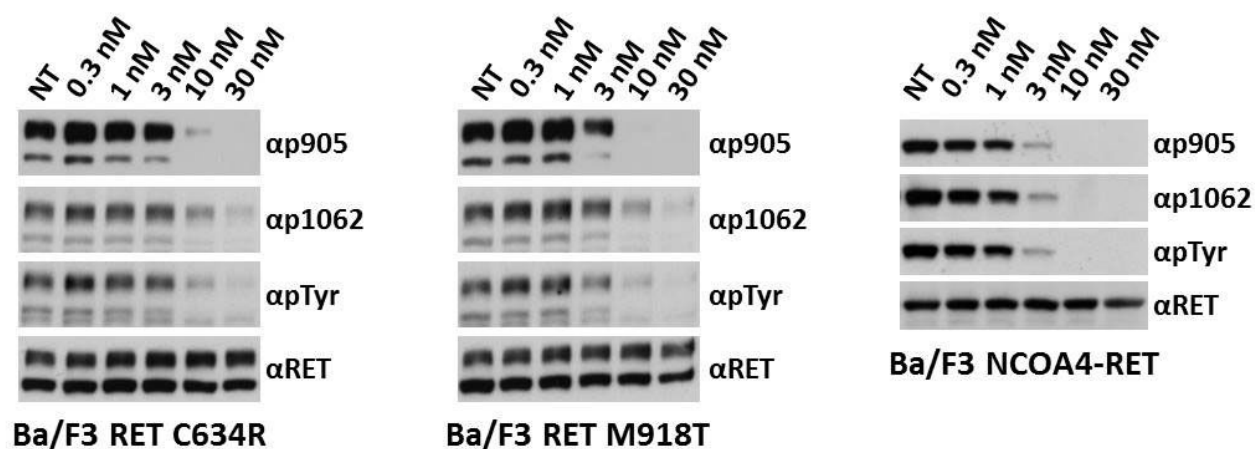
Supplementary Figure S3: RET, TRKA and CSF1R kinase inhibition by NPA101.3



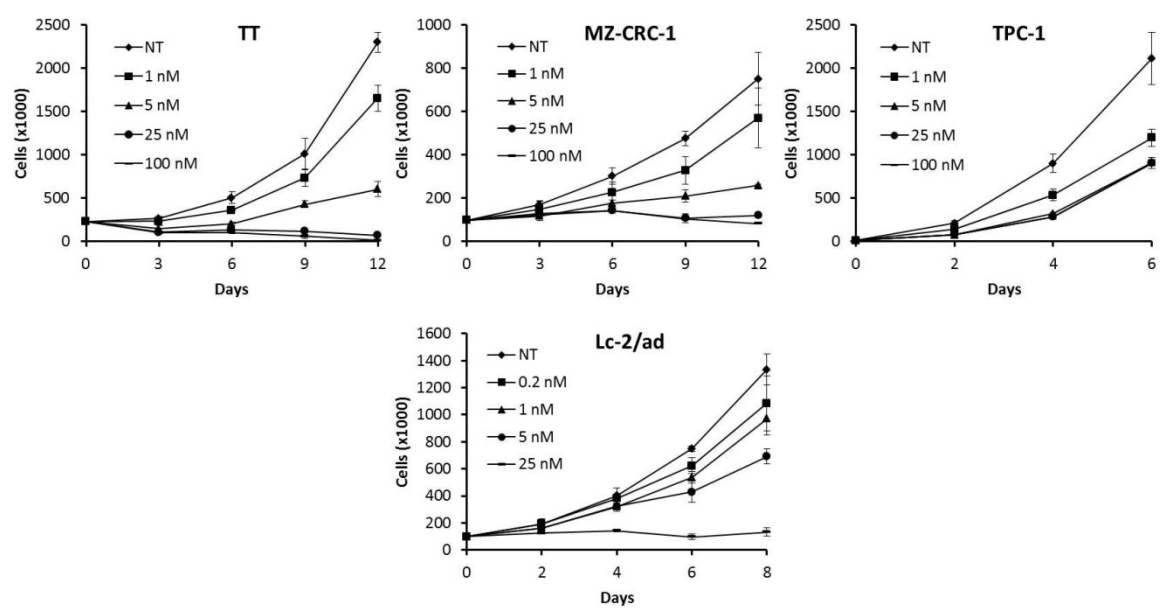
Supplementary Figure S4: NPA101.3-mediated inhibition of phosphorylation and signalling of oncogenic RET proteins endogenously expressed in human cancer cells — Serum-starved RET mutant human cancer cell lines were treated for 2 hours with the indicated concentrations of the drug. Total cell lysates (50 μ g) were subjected to immunoblotting with α p1062 RET, anti-phospho-MAPK (α pMAPK) and anti-phospho-SHC (α pSHC) antibodies. The blots were normalized using anti-RET (α RET), anti-MAPK (α MAPK) and anti-SHC (α SHC).



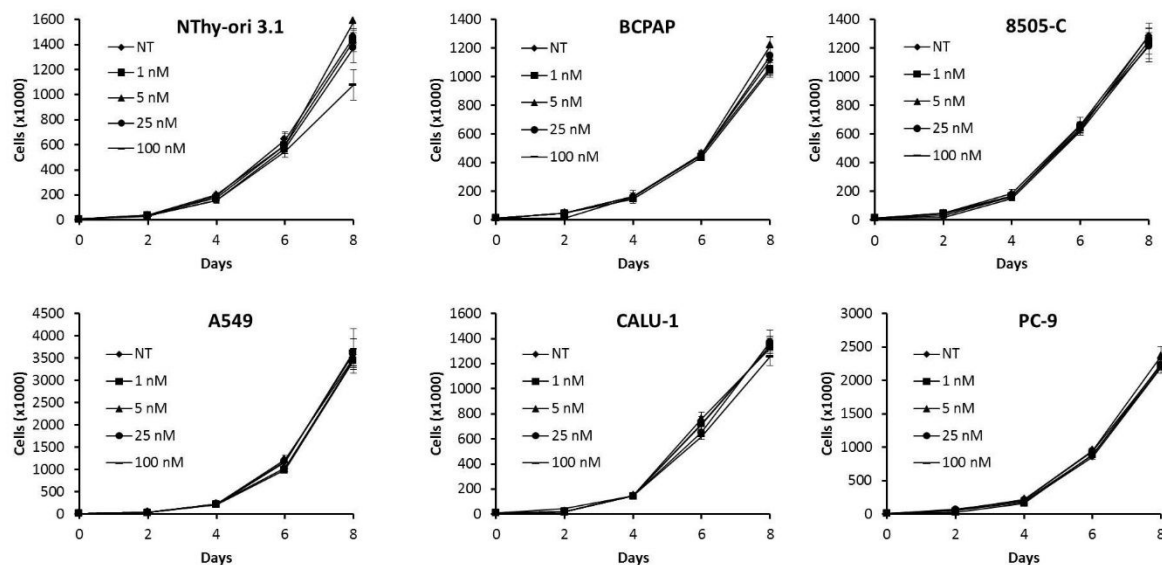
Supplementary Figure S5: Effects of NPA101.3 on RAS/MAPK signalling pathway in RET-negative human cancer cells — The indicated cell lines were serum-starved and treated for 2 hours with indicated concentrations of the drug. Total cell lysates (50 µg) were subjected to immunoblotting with indicated antibodies.



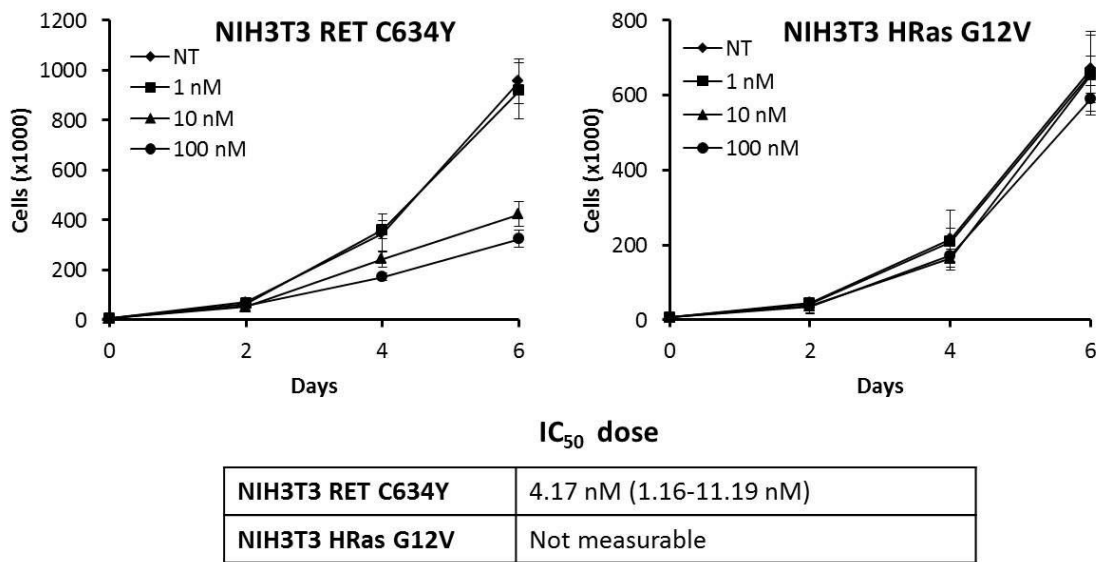
Supplementary Figure S6: NPA101.3-mediated inhibition of phosphorylation of oncogenic RET proteins expressed in Ba/F3 cells — The indicated Ba/F3 transfectants were serum starved and treated for 2 hours with the indicated concentrations of the drug. Total cell lysates (50 μ g) were subjected to immunoblotting with indicated antibodies.



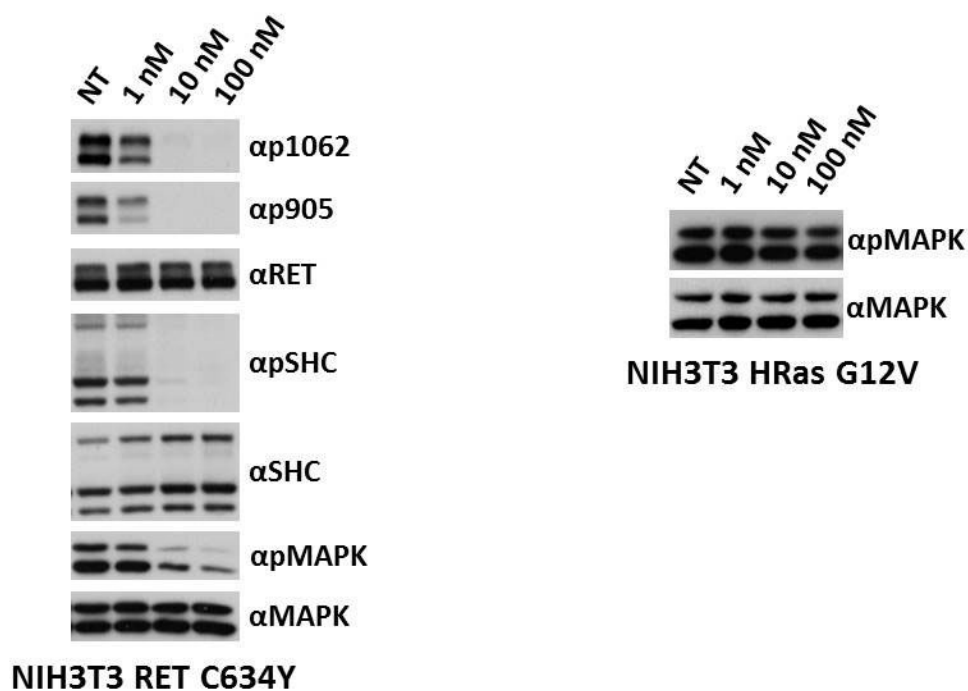
Supplementary Figure S7: NPA101.3-mediated inhibition of proliferation of RET mutant thyroid and lung cancer cells — The indicated cell lines were incubated with vehicle (NT: not treated) or the indicated concentrations of the compound and counted at the indicated time points. Data are the mean \pm SD of a single experiment performed in triplicate.



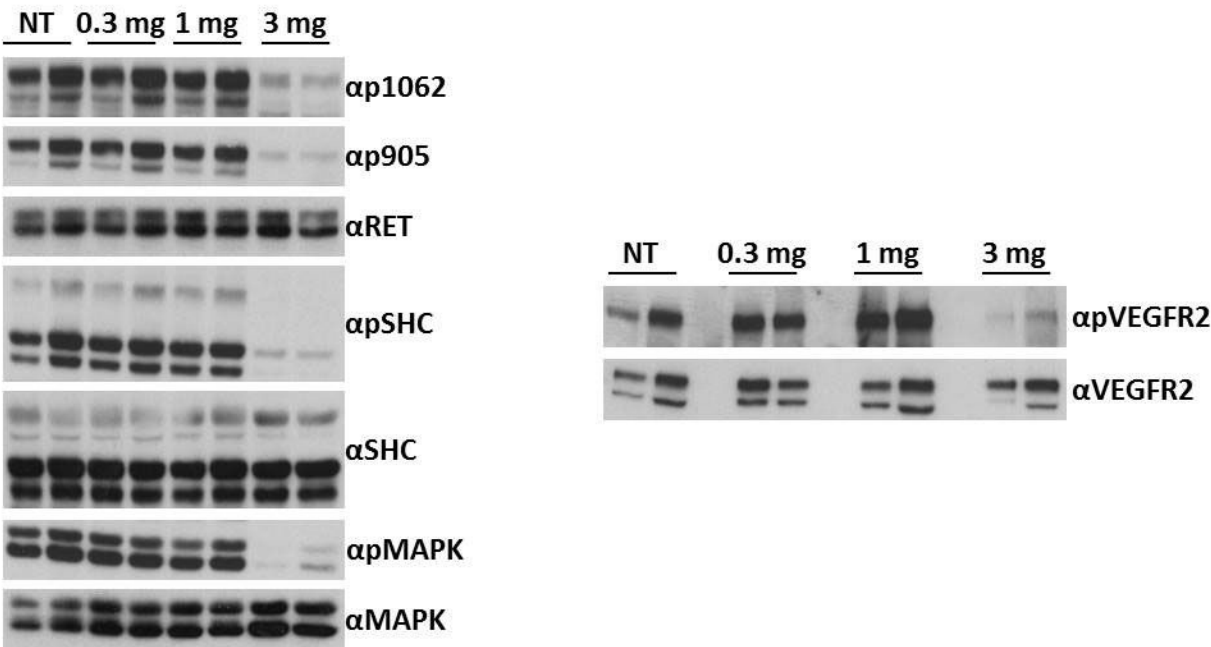
Supplementary Figure S8: Effects of NPA101.3 on proliferation of RET-negative cancer cells — The indicated cell lines were incubated with vehicle (NT: not treated) or the indicated concentrations of the compound and counted at the indicated time points. Data are the mean \pm SD of a single experiment performed in triplicate.



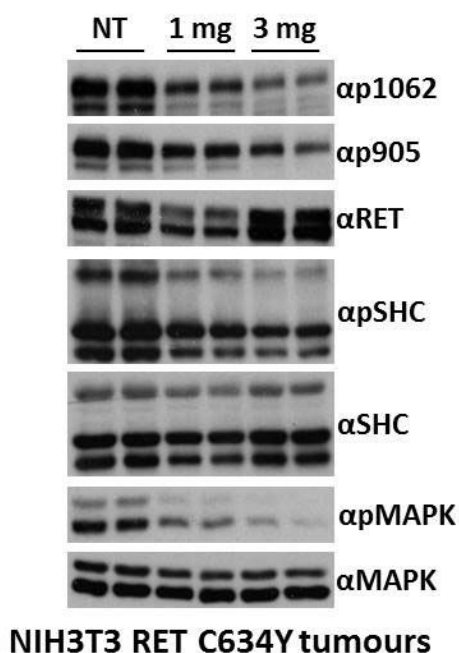
Supplementary Figure S9: NPA101.3-mediated inhibition of proliferation of RET-transformed NIH3T3 cells — Serum-starved NIH3T3 cells exogenously expressing the RET/C634Y or HRAS/G12V oncogenes were incubated with vehicle (NT: not treated) or the indicated concentrations of the compound and counted at the indicated time points. Data are the mean \pm SD of a single experiment performed in triplicate. Growth inhibition IC₅₀ doses of the compound are reported. 95% CI are indicated in brackets.



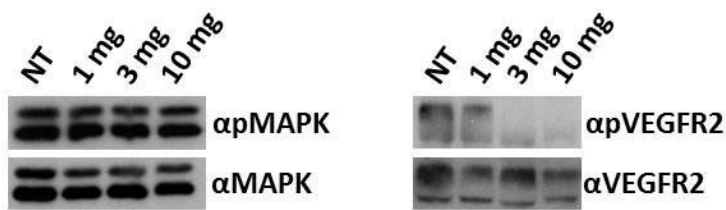
Supplementary Figure S10: NPA101.3-mediated inhibition of phosphorylation and signalling of oncogenic RET proteins expressed in NIH3T3 cells — Serum-starved RET/C634Y or HRAS/G12V-transformed NIH3T3 cells were treated for 2 hours with the indicated concentrations of the drug. Total cell lysates (50 μ g) were subjected to immunoblotting with with indicated antibodies.



Supplementary Figure S11: *In vivo* target inhibition of NPA101.3 in nude mice implanted with cells transformed by RET/C634Y — NIH3T3 RET/C634Y cells (2×10^5) were inoculated subcutaneously into the right and left dorsal portions of nude mice. When tumours reached approximately $\sim 200 \text{ mm}^3$, mice (2 mice/dose) were treated by oral gavage with 3 doses (0, 24, 48 h) of the compound (0.3, 1 and 3 mg/Kg) or left untreated (NT); proteins were harvested 3 h after the last dose. Left) Total lysates (50 μg) from 2 representative NIH3T3 RET/C634Y tumours for each dose were immunoblotted with indicated antibodies. Right) Total lysates (1 mg) from 2 representative NIH3T3 RET/C634Y tumours for each dose were subjected to VEGFR2 immunoprecipitation followed by Western blotting with anti-phospho-VEGFR2 antibody ($\alpha\text{pVEGFR2}$). The blots were normalized using anti-VEGFR2 (αVEGFR2).

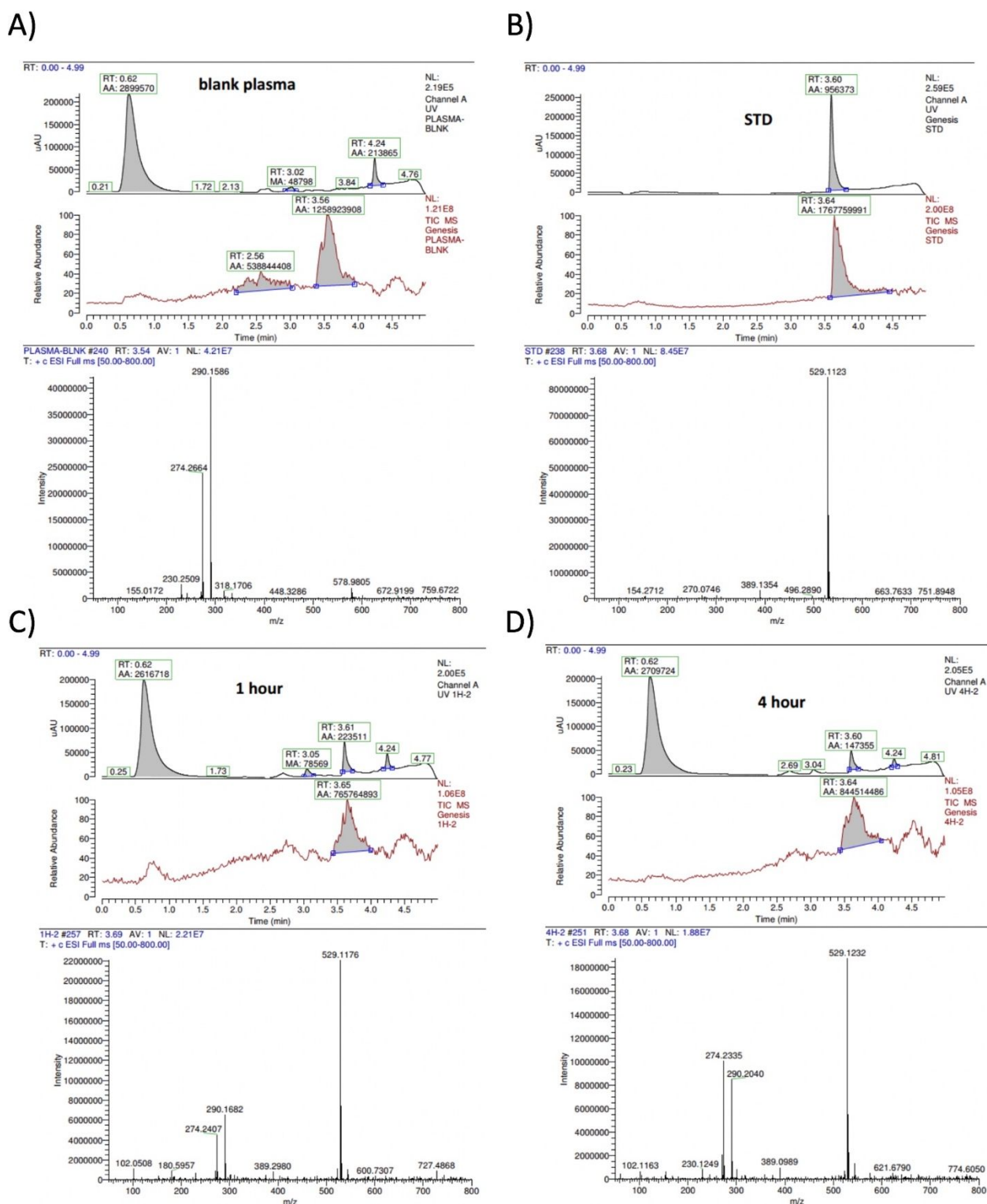


Supplementary Figure S12: Effects of NPA101.3 on cellular phosphorylation events in nude mice implanted with NIH3T3 cells transformed by RET/C634Y — Three hours after the last dose, 2 representative tumours for each dose from the experiment reported in Figure 6 were harvested from mice treated with indicated doses of NPA101.3 or left untreated (NT). Proteins were extracted and total protein lysates (50 µg) were immunoblotted with indicated antibodies.

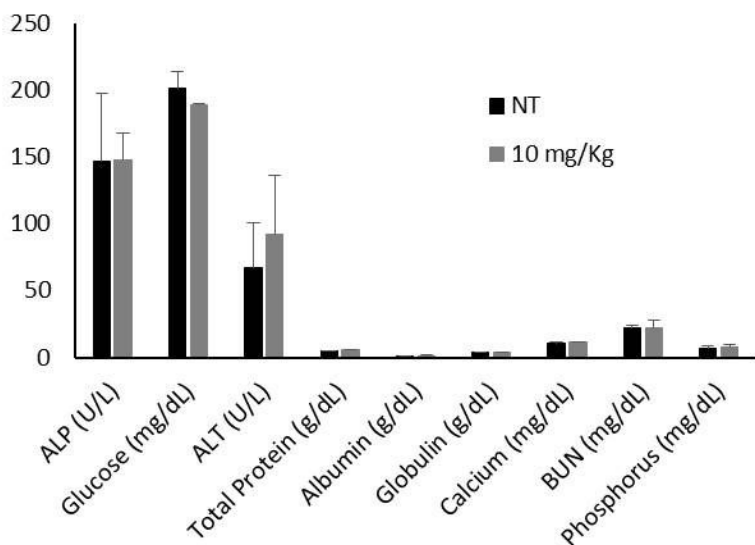


NIH3T3 HRas G12V tumours

Supplementary Figure S13: Effects of NPA101.3 on cellular phosphorylation events in nude mice implanted with NIH3T3 cells transformed by HRAS/G12V—Three hours after the last dose, one representative tumour for each indicated dose from the experiment reported in Figure 6 was harvested and proteins were extracted. Left) total protein lysates (50 μ g) were immunoblotted with indicated antibodies. Right) protein extracts (1 mg) were subjected to VEGFR2 immunoprecipitation followed by Western blotting with anti-phospho-VEGFR2 antibody (α pVEGFR2). The blots were normalized using α VEGFR2.



Supplementary Figure S14: *In vivo* metabolism study. NPA101.3 was orally dosed (10 mg/kg) to mice (one animal for each point). Blood plasma samples were collected at 1 h and 4 h after dosing; blood from one untreated mouse (blank) and NPA101.3 solution (STD: standard) were used as controls. NPA101.3 drug peak was detected at 3.61 min ($m/z = 529$) at either time point. No trace of the de-methyl metabolite at $m/z = 515$ was observed. The m/z 279 and 290 were not specific peaks identified also in the blank plasma sample.



Supplementary Figure S15: Biochemical analysis. Plasma concentration of Alkaline Phosphatase (ALP), Glucose (GLU), Alanine Transaminase (AST), Total Protein (T.Prot.), Albumin (ALB), Globulins (Glo), Calcium (Cal), Blood Urea Nitrogen (BUN) and Phosphorus (PHO) were measured upon treating animals with NPA101.3 (10 mg/kg/day) for 7 days or vehicle as indicated (4 animals for each group).